

1 **Exploring the ENSO Modulation of the QBO Periods with GISS E2.2 Models**

2 Tiehan Zhou<sup>1,2</sup>, Kevin J. DallaSanta<sup>1,3</sup>, Clara Orbe<sup>1,3</sup>, David H. Rind<sup>1</sup>, Jeffrey A. Jonas<sup>1,2</sup>,

3 Larissa Nazarenko<sup>1,2</sup>, Gavin A. Schmidt<sup>1</sup>, Gary Russell<sup>1</sup>

4

5 <sup>1</sup>NASA Goddard Institute for Space Studies, New York, NY 10025, USA

6 <sup>2</sup>Center for Climate Systems Research, Columbia University, New York, NY 10025, USA

7 <sup>3</sup>Department of Applied Physics and Applied Mathematics, Columbia University, New York, NY 100-  
8 25, USA

9

10 Correspondence to: Tiehan Zhou (tz2131@columbia.edu)

11

12 **Abstract.** Observational studies have shown that the El Niño–Southern Oscillation (ENSO) exerts  
13 an influence on the Quasi-Biennial Oscillation (QBO). The downward propagation of the QBO tends to  
14 speed up and slow down during El Niño and La Niña, respectively. Recent results from general  
15 circulation models have indicated that the ENSO modulation of the QBO requires a relatively high  
16 horizontal resolution, and that it does not show up in the climate models with parameterized but  
17 temporally constant gravity wave sources. Here, we demonstrate that the NASA GISS E2.2 models can  
18 capture the observed ENSO modulation of the QBO period with a horizontal resolution of 2° latitude by  
19 2.5° longitude but with its gravity wave sources being parameterized interactively. This is because El  
20 Niño events lead to more vigorous gravity wave sources generating more absolute momentum fluxes  
21 over the equatorial belt, as well as less filtering of these waves into the tropical lower stratosphere  
22 through a weakening of the Walker circulation. Various components of the ENSO system such as the  
23 SSTs, the convective activities, and the Walker circulation are intimately involved in the generation and  
24 propagation of parameterized gravity waves, through which ENSO modulates the QBO period in GISS  
25 E2.2 models.

26 **1. Introduction**

27 The QBO dominates the interannual variability in the tropical stratosphere (Baldwin et al., 2001)  
28 while ENSO is the primary mode of interseasonal–interannual variability over the tropical Pacific Ocean  
29 (Wang et al., 2016). It is well-known that both the QBO and the ENSO have far-reaching implications  
30 for global weather and climate systems (Hamilton et al., 2015; Philander, 1990; Sarachik and Cane, 2010;  
31 Domeisen et al., 2019).

32 The QBO and the ENSO defy linear relationships (Angell, 1986; Xu, 1992; Hu et al., 2012) as  
33 highlighted by that fact that while the QBO and ENSO indices are negatively correlated before 1980s  
34 and positively correlated after 1980s (Garfinkel and Hartmann, 2007; Domeisen et al., 2019; Rao et al.,  
35 2020c) they are virtually uncorrelated over the longer periods from 1953 to recent times (Garfinkel and  
36 Hartmann, 2007; Geller et al., 2016b, see their Figure 5 for details). However, Maruyama and Tsuneoka  
37 (1988) spotted an intriguing connection between the anomalously short easterly phase of the QBO at 50  
38 hPa in 1987 and the El Niño event that persisted through that year. Based on the results from a  
39 mechanistic model, Geller et. al (1997) suggested that the equatorial sea surface temperatures (SST)  
40 modulate the wave momentum fluxes into the stratosphere and thus the QBO. Remarkably, an  
41 observational study conducted by Taguchi (2010) demonstrated that the downward propagation of the  
42 QBO tends to speed up during El Niño and slow down during La Niña while the amplitude of the QBO  
43 tends to be smaller during El Niño and larger during La Niña, respectively. Using radiosonde data from  
44 10 near-equatorial stations distributed along the Equator, Yuan et al. (2014) found that the ENSO  
45 modulation of the QBO period is more robust than that of the QBO amplitude, which is likely due to the  
46 fact that the QBO periods are characterized by a high degree of zonal uniformity whereas the QBO  
47 amplitudes exhibit the zonal asymmetries of about 10% (Hamilton et al., 2004, see their Fig. 15).

Deleted: because of the apparent cancelation

49 The QBO influences the distribution and transport of various chemical constituents (Zawodny and  
50 McCormick, 1991; Trepte and Hitchman, 1992; Hasebe, 1994; Kawatani et al., 2014), the extratropical  
51 circulation in the winter stratosphere (Holton and Tan, 1980; Labitzke, 1982; Rao et al., 2020a, 2020b,  
52 2021), tropical moist convection (Collimore et al., 2003; Liess and Geller, 2012), the activities of tropical  
53 cyclones (Gray et al., 1984; Ho et al., 2009), the ENSO (Gray et al., 1992; Huang et al., 2012; Hansen  
54 et al. 2016), the Hadley circulation (Hitchman and Huesmann, 2009), the tropospheric subtropical jet  
55 (Garfinkel and Hartmann, 2011a, 2011b; Kumar et al., 2022), the boreal summer monsoon (Giorgetta et  
56 al., 1999; Yoden et. al 2023), and the Madden-Julian Oscillation (Yoo and Son, 2016). Thus, it is  
57 imperative that weather and climate models have the capacity to simulate the ENSO modulation of the  
58 QBO.

59 Various studies have investigated how the ENSO exerts its influence over the QBO in climate models.  
60 Schirber (2015) conducted two sets of experiments to explore this issue using the general circulation  
61 model European Centre/Hamburg 6 (ECHAM6) wherein a convection-based gravity wave (GW) scheme  
62 was newly implemented. The first set of experiments was called QBOW where the initial QBO  
63 configurations consisted of a westerly jet above the 10 hPa level and an easterly jet below that level.  
64 Likewise, in the second set of experiments named as QBOE, the initial QBO conditions included an  
65 easterly and westerly jet above and below the 10 hPa level, respectively. Schirber showed that for QBOW,  
66 the ensemble mean period of the QBO from the El Niño runs is shorter than that from the La Niña runs  
67 while for QBOE, the ensemble mean periods are comparable between the El Niño and the La Niña runs.  
68 Schirber also noted that there is no systematic change in amplitude of the QBO jets between El Niño and  
69 La Niña runs. Using version 3 of the EC-Earth Consortium's climate model with a triangular spectral  
70 truncation at total wavenumber 255 (T255, horizontal resolution of  $\sim 0.54^\circ$ ), Christiansen et al. (2016)  
71 reported that each of ten ensemble members simulated a faster QBO descent rate during El Niño than

72 during La Niña, and that their ensemble mean QBO phase speeds were comparable to those derived from  
73 the reanalyses.

74 Employing two atmospheric general circulation models (AGCM) developed under the Model for  
75 Interdisciplinary Research on Climate (MIROC) framework, Kawatani et al. (2019) investigated the  
76 possible mechanism of the ENSO modulation of the QBO. They first compared a 100-year perpetual El  
77 Niño run with a 100-year perpetual La Niña run from the MIROC-AGCM with T106 horizontal  
78 resolution and 500-m vertical spacing in the stratosphere without any nonorographic GW  
79 parameterizations. Then they repeated the two AMIP-style perpetual El Niño and La Niña experiments  
80 but using the atmospheric part of the Model for Interdisciplinary Research on Climate, Earth System  
81 Model (MIROC-ESM) with T42 horizontal resolution and 700-m vertical spacing in the stratosphere  
82 where the effects of nonorographic GWs are parameterized and the GW sources are held constant in  
83 time. They found that the MIROC-AGCM simulates shorter QBO periods during El Niño than during  
84 La Niña because of the larger equatorial vertical wave fluxes of zonal momentum in the uppermost  
85 troposphere and consequently the much larger resolved GW forcing in the stratosphere during warm  
86 ENSO phase. However, they found almost no difference in the average QBO periods simulated by the  
87 MIROC-ESM between El Niño and La Niña because the QBO was generated by the parameterized  
88 nonorographic GW forcing in the model where the GW sources were held constant in time, thus did not  
89 respond to the SST changes associated with the ENSO cycle (See their Figs. 16 and 18 for more details).

90 Using more than a dozen of models from five modeling centers with their horizontal resolutions  
91 ranging from T42 ( $\sim 2.79^\circ$ ) to T1279 ( $\sim 0.14^\circ$ ), Serva et al. (2020) found that a relatively high horizontal  
92 resolution above T159 ( $\sim 0.75^\circ$ ) was desirable to simulate the observed modulation of the QBO descent  
93 rate under strong ENSO events, while the amplitude response is generally weak at any horizontal  
94 resolution. They also pointed out that over-dependence on parameterizing the effects of GWs with

95 temporally invariant sources is detrimental to the realistic simulation of the coupling between the ocean  
96 and the tropical stratosphere in current climate models.

97 As far as the ENSO modulation of the QBO period is concerned, both Kawatani et al. (2019) and  
98 Serva et al. (2020) emphasized the importance of a relatively high horizontal resolution and the  
99 inadequacy of non-interactive GW sources. However, the exploratory work of Schirber (2015) shows  
100 that the ENSO modulation of the QBO period can, to some extent, be simulated in the GCM ECHAM6  
101 with T63 and an associated Gaussian grid of  $\sim 1.9^\circ$  horizontal resolution because rather than being held  
102 constant in time, the properties of non-interactive GW sources in the tropics are determined by the  
103 simulated convection which is modulated by ENSO phases.

104 Rind et al. (1988) pioneered the use of meteorologically interactive GW sources in the Goddard  
105 Institute for Space Studies (GISS) climate models. These sources included flow over topography,  
106 convection, wind shear, and, in Rind et al. (2007), wind deformation. By increasing the vertical  
107 resolution and revising the formulations, various versions of the GISS models subsequently simulate a  
108 spontaneous QBO (Rind et al., 2014, 2020; DallaSanta et al., 2021). The GISS E2.2 models are  
109 comprehensive climate models optimized for the middle atmosphere (Rind et al., 2020; Orbe et al., 2020).  
110 Their outputs have been submitted to the archive of the Coupled Model Intercomparison Project Phase  
111 6 (CMIP6). Bushell et al. (2020) pointed out that most of current climate models are highly dependent  
112 on parameterized nonorographic GW forcing to simulate a QBO. Unsurprisingly, DallaSanta et al. (2021)  
113 found that the parameterized convective GWs play a dominant role in generating the spontaneous QBO  
114 in the GISS E2.2 models.

115 High-resolution AGCMs can realistically simulate atmospheric structure without resorting to  
116 parameterized GWs (e.g., Watanabe et al., 2008), but the associated computational cost is too high for  
117 the Earth system modeling at the present time. Thus, most climate models still require GW

118 parameterization schemes. What is more, Fig. 4(c) in Serva et al. (2020) shows that two different GW  
119 parameterization schemes employed by the same T255 model make a drastic difference in the ENSO  
120 modulation of the QBO period. Specifically, one scheme makes a difference of about 10 months in the  
121 ensemble mean QBO period between El Niño and La Niña episodes while the other hardly makes an  
122 appreciable difference. In other words, improperly parameterized GW forcing could destructively  
123 interfere with the ENSO modulation of the QBO period in high-resolution climate models. Therefore, it  
124 is imperative that GWs forcing be parameterized properly in climate models with a variety of horizontal  
125 resolutions.

126 In this paper, we will evaluate the ENSO modulation of the QBO simulated by the GISS E2.2 models  
127 against the observed and explore how the ENSO modulates the QBO period in those models. Section 2  
128 describes the observations and GISS E2.2 models used in this study and outlines our methods of analyses.  
129 Section 3 revisits the ENSO modulation of the QBO from the observational point of view. Section 4  
130 evaluates the ENSO modulation of QBO period in the historical runs simulated by four versions of the  
131 GISS E2.2 models. Section 5 explores the physical mechanisms underlying the simulated modulation.  
132 Conclusions and discussion are presented in section 6.

133

## 134 **2. Observations, model simulations, and methods**

### 135 **2.1 Observations**

136 To study the observed QBO, we use the monthly mean zonal winds provided by Free University of  
137 Berlin (FUB). The FUB data were produced by combining the radiosonde observations at the following  
138 three equatorial stations: Canton Island near 172°W, 3°S (closed in 1967), Gan/Maledive Islands near  
139 73°E, 1°S (closed in 1975), and Singapore near 104°E, 1°N (Naujokat, 1986). We use 63 years (i.e., 756

140 months) of the FUB data ranging from 1953 to 2015 at the following seven pressure levels: 70, 50, 40,  
141 30, 20, 15, and 10 hPa.

142 The observed ENSO index is derived from the National Oceanic and Atmospheric Administration  
143 (NOAA) Extended Reconstructed SST (ERSST) V5 datasets (Huang et al., 2017) provided by National  
144 Centers for Environmental Information (NCEI). ERSST produced on a  $2^\circ \times 2^\circ$  grid is derived from the  
145 International Comprehensive Ocean-Atmosphere Data Set (ICOADS). The latest version of ERSST,  
146 version 5, uses new datasets from ICOADS Release 3.0 SST, combining information from Argo floats  
147 above 5 m and Hadley Centre Ice-SST version 2 ice concentrations.

148 The monthly Outgoing Longwave Radiation (OLR) on a  $2.5^\circ \times 2.5^\circ$  grid from NCEI is used as a  
149 proxy for tropical convection since cloud top temperatures are negatively correlated with cloud height  
150 in the tropics (Salby, 2012). The ERA5 (Hersbach et al., 2020) monthly mean zonal winds were  
151 employed to depict the observed Walker circulation against which we evaluate those simulated by GISS  
152 E2.2 models. The employed OLR and zonal winds range from 1979 to 2015.

### 153 **2.2 Description of the models and simulations**

154 GISS E2.2 is a climate model specially optimized for the middle atmosphere (Rind et al., 2020; Orbe  
155 et al., 2020) and its output was submitted to the Coupled Model Intercomparison Project Phase 6 (CMIP6)  
156 archive. The horizontal resolution of all GISS E2.2 models is  $2^\circ$  (latitude)  $\times$   $2.5^\circ$  (longitude) for the  
157 atmosphere and the model extends from the surface to 0.002 hPa (~89 km) with 102 vertical layers (for  
158 more details, see Table 1 in Rind et al., 2020). Note that an adequate vertical resolution is necessary for  
159 climate models to internally generate a spontaneous QBO (Scaife et al., 2000; Richter et al. 2014; Rind  
160 et al, 2014, 2020; Geller et al. 2016a; Butchart et al. 2018).

161 According to [atmospheric chemistry](#), the atmospheric component of the GISS E2.2 models was  
162 configured in two ways for CMIP6. The first configuration is denoted as NonINTERactive (NINT) where

Deleted: composition interactivity

Deleted: "

Deleted: "

166 the fields of radiatively active components such as ozone and multiple aerosol species are specified from  
167 previously calculated offline fields (Kelley et al. 2020; Miller et al., 2021). The second configuration  
168 includes interactive gas-phase chemistry and a mass-based (One-Moment Aerosol, OMA) aerosol  
169 module, where aerosols and ozone are driven by emissions and calculated prognostically (Bauer et al.,  
170 2020; Nazarenko et al., 2022). The abovementioned NINT and OMA configurations correspond to  
171 physics-version=1 (“p1”) and physics-version=3 (“p3”), respectively, in the CMIP6 archive.

172 The basic dynamics and tropospheric physics structure of the GISS E2.2 models were based on the  
173 GISS E2.1 model (Kelley et al., 2020). One version of the cloud parameterization schemes used in E2.2,  
174 termed as “standard physics” (SP), has not been fully upgraded to the state-of-the-art module customized  
175 for E2.1 which has only 40 vertical layers up to 0.1 hPa (Rind et al., 2020). Accordingly, E2.2–SP has a  
176 younger sibling, E2.2–AP, whose cloud parameterization schemes, termed as “Altered Physics” (AP),  
177 are more aligned with those in E2.1 and whose outputs were thus favored for the submission to the  
178 CMIP6 archive. “Altered Physics” in E2.2–AP brings about a somewhat different response to SST as  
179 compared with the “standard physics” in E2.2–SP.

180 The QBO in the GISS models are mainly driven by GWs (DallaSanta et al., 2021). The phase  
181 velocities and momentum fluxes of GW sources are coupled to convective cloud-top-pressure altitudes,  
182 convective mass fluxes, background wind fields, etc. (Rind et al., 1988, 2014, 2020). Specifically  
183 speaking, intrinsic phase velocities  $\pm 10 \text{ m s}^{-1}$  and  $\pm 20 \text{ m s}^{-1}$  of GWs generated by convection are  
184 Doppler-shifted by local background winds for shallow convection and for convection penetrating above  
185 the altitudes of the 400-hPa pressure level, respectively. Convective gravity wave momentum flux  
186 magnitude is determined by the density and Brunt-Vaisala frequency at the top of convective region and  
187 the vertically integrated mass flux over the convective region. The mass flux in the model is strongly  
188 related to the depth of penetration, and thus this parameterization is somewhat similar to that of the other

Deleted: , which will be discussed further below



190 models that use convective sources (see Eq. 7 in Rind et al., 1988 and the further discussion in Rind et  
191 al., 2014).

192 Using the same GW parameterization scheme, both E2.2–SP and E2.2–AP are included in this study  
193 to gain insight into the mechanisms through which ENSO modulates the QBO period despite the fact  
194 that the outputs of E2.2–SP were not submitted to the CMIP6 archive.

195 We will look into two atmosphere-only (AMIP) ensemble simulations where the evolution of SST  
196 and sea ice fraction (SIF) is specified and two coupled ensembles where the respective model atmosphere  
197 interacts with the ocean component termed as the GISS Ocean v1 (GO1) which extends from the surface  
198 to the ocean floor with 40 vertical layers and has a horizontal resolution of 1° latitude by 1.25° longitude  
199 (Schmidt, et al., 2014; Kelley et al., 2020). Table 1 lists the four model configurations and their respective  
200 ensemble simulations investigated in this study.

201 The first two ensembles in Table 1 were generated by AMIP–OMA–SP and AMIP–OMA–AP models  
202 where the SST and SIF from the HadISST1 dataset (Rayner et al., 2003) were prescribed for the  
203 simulations between 1870 and 2014 while their climatological annual cycles over the 1876–1885 period  
204 were specified for the earlier simulations between 1850 and 1869. Both AMIP–OMA–SP and AMIP–  
205 OMA–AP prognostically calculate the concentrations of ozone, methane, chlorofluorocarbons, aerosols,  
206 etc. The main differences between AMIP–OMA–SP and AMIP–OMA–AP reside in the package of cloud  
207 parameterization schemes, which leads to their different responses to SST and thus may have important  
208 implications for simulating the ENSO modulation of the QBO period. We discarded the simulations  
209 ranging from 1850 to 1869 in this study because they are irrelevant to the ENSO modulation of the QBO  
210 in the absence of interannual variations in the prescribed SST over that period. Note that the two extended  
211 historical AMIP simulations from 1870 to 2014 listed in Table 1 were not submitted to the CMIP6  
212 archive. However, AMIP–OMA–AP did generate a 5-member ensemble over the 1979–2014 period that

**Deleted:** Note that outputs from E2.2–SP models, following the CMIP6 protocol and naming, are available from the NASA Center for Climate Simulation (NCCS) portal (under the title E2.2.1).

**Deleted:** In this study we

**Deleted:** imposed

219 was submitted to the CMIP6 archive and tagged as E2-2-G.amip.r[1-5]i1p3f1. It is worth noting that the  
220 climatological characteristics over the 1979–2014 period derived from the AMIP–OMA–AP ensemble  
221 listed in Table 1 are comparable to those derived from E2-2-G.amip.r[1-5]i1p3f1 albeit the climate  
222 trajectories of the individual ensemble members over the 1979–2014 period are expected to differ  
223 between those two ensembles starting from January 1850 and January 1979, respectively, due to the  
224 chaotic nature of climate systems.

225 The other two ensembles in Table 1 were generated by the Coupled–NINT–SP and Coupled–NINT–  
226 AP where the respective atmospheric components are coupled with GO1. Both the Coupled–NINT–SP  
227 and Coupled–NINT–AP simulations were performed with the prescribed atmospheric composition  
228 generated from the AMIP-style OMA simulations using the historical forcings over the 1850–2014  
229 period. As mentioned earlier with regard to the AMIP–OMA–SP and AMIP–OMA–AP runs, the  
230 difference in cloud physics between the Coupled–NINT–SP and Coupled–NINT–AP models is exploited  
231 to gain a deeper insight into the mechanisms through which the ENSO modulates the QBO periods. Both  
232 Coupled–NINT–SP and Coupled–NINT–AP ensemble runs started from January 1850 and ended in  
233 December 2014.

234 Since there are no interannual variations in the prescribed SST over the 1850–1869 period for both  
235 the AMIP–OMA–SP and AMIP–OMA–AP runs, our analyses focus on the 1870–2014 period for those  
236 two ensembles. For the sake of conciseness and consistency, we also discarded the outputs from two  
237 coupled runs over the 1850–1869 period. In short, we only use the data over the 1870–2014 period from  
238 the ensemble simulations listed in Table 1.

## 239 **2.3 Methods**

### 240 **2.3.1 Data processing**

241 We first fill the missing FUB zonal winds at the 10 hPa level for the first 3 years by linear  
242 extrapolation in log-pressure height. Then, we remove the climatological mean zonal winds from the  
243 observed to obtain the monthly anomalies of zonal winds. These anomalous monthly zonal winds will  
244 be used for our observational study in this paper.

245 To obtain the ENSO index from the ERSSTv5 data ranging from 1953 to 2015, we use the same  
246 method to calculate the Oceanic Niño Index (ONI) as the Climate Prediction Center (CPC) of NOAA.  
247 Namely, the ONI is defined as a 3-month running mean of ERSSTv5 SST anomalies in the Niño 3.4  
248 region (5°S–5°N, 120°–170°W) based on centered 30-year base periods updated every 5 years  
249 ([https://origin.cpc.ncep.noaa.gov/products/analysis\\_monitoring/ensostuff/ONI\\_v5.php](https://origin.cpc.ncep.noaa.gov/products/analysis_monitoring/ensostuff/ONI_v5.php)). This method  
250 ensures a proper identification of El Niño and La Niña by taking the secular changes in SSTs into account.

251 The SST anomalies (SSTA) are defined as the deviations of the SST from its climatological annual cycle  
252 over a selected base period. Specifically, the SSTA during 1951–1955 are based on the 1936–1965 base  
253 period; the SSTA during 1956–1960 are based on the 1941–1970 base period; and so on. Thus, as the  
254 CPC of NOAA we used the ERSSTv5 SST from January 1936 to January 2016 period to obtain the ONI  
255 from January 1953 to December 2015.

256 Following the CPC of NOAA, we refer to El Niño or La Niña episodes as the periods when the ONIs  
257 are greater than +0.5°C or less than –0.5°C for at least five consecutive months, respectively. Since the  
258 temperature measurement is only accurate to the tenths place, all our calculated ONIs are rounded to the  
259 nearest tenth. Based on the rounded ONIs, our identified El Niño and La Niña episodes are almost  
260 identical to those listed at the abovementioned website of NOAA CPC. Accordingly, we identified 21  
261 El Niño and 15 La Niña events between 1953 and 2015.

262 Similarly, when we explore how GISS E2.2 models simulate the ENSO modulation of the QBO we  
263 define the ONI as a 3-month running mean of prescribed SSTA from the AMIP–OMA–SP and AMIP–

Deleted: SST anomalies

Deleted: SST anomalies

Deleted: SST anomalies

267 OMA-AP runs, or simulated SSTA from the Coupled-NINT-SP and Coupled-NINT-AP runs in the  
268 Niño 3.4 region (5°S- 5°N, 120°- 170°W) based on centered 30-year base periods updated every 5 years.  
269 Here, the SSTA are also defined as the deviations of the SST from its climatological annual cycle over  
270 a selected base period. Specifically, the SSTA during 1886-1890 are based on the 1871-1900 base  
271 period; the SSTA during 1891-1895 are based on the 1876-1905 base period; the SSTA during 1991-  
272 1995 are based on the 1976-2005 base period; the SSTA during 1996-2000 are based on the 1981-2010  
273 base period. In addition, the SSTA during the earliest 1870-1885 and latest 2011-2014 spans are ad hoc  
274 based on the 1870-1899 and 1985-2014 base periods, respectively. Thus, we used the specified or  
275 simulated SSTs over the 1870-2014 period to obtain the ONI from February 1870 to November 2014.

276 For the sake of consistency, we also apply this same filtering procedure to all other fields simulated  
277 by GISS E2.2 models such as OLR, zonal winds, resolved wave forcing, parameterized GW forcing,  
278 absolute convective momentum flux, etc. Thus, the simulated zonal winds and other quantities were  
279 subjected to a 3-month moving averaging. In addition, the secular trends of zonal winds and those other  
280 quantities were also removed due to the adoption of the consecutive 5-year base periods. To further  
281 simplify our analyses, all processed model outputs used in this study range from 1871 to 2013. In other  
282 words, we also discarded the processed model outputs over the period between February 1870 to  
283 December 1870 and that between January 2014 to November 2014.

284 Employing the above-mentioned criterion that was used to identify the observed ENSO events  
285 between 1953 and 2015, we identified 34 El Niño and 30 La Niña events over the period from 1871 to  
286 2013 from the specified HadISST1 dataset. We further found that the five members of the Coupled-  
287 NINT-SP ensemble simulations generated 31, 31, 29, 35, and 36 El Niño events and produced 34, 34,  
288 35, 37, and 35 La Niña events, respectively, over the period from 1871 to 2013. In parallel, we identified

Deleted: SST anomalies

Deleted: SST anomalies

Deleted: SST anomalies

Deleted: SST anomalies

Deleted: SST anomalies

Deleted: SST anomalies

Deleted: SST anomalies

296 37, 42, 40, 37, and 38 El Niño events and 38, 43, 37, 40, and 39 La Niña events from the SSTs simulated  
297 by the five members of the Coupled–NINT–AP ensemble, respectively, over the same period.

### 298 **2.3.2 Statistical analysis**

299 Following Wallace et al. (1993), we decompose the zonal winds from both the observed and the  
300 simulated between 10 and 70 hPa pressure levels into two leading pairs of empirical orthogonal functions  
301 (EOFs) and principal components (PCs) because they typically account for more than 90% of the vertical  
302 structure variance (Wallace et al., 1993; DallaSanta et al., 2021). For the sake of robustness, we excluded  
303 the FUB data after 2015 because the first two EOFs explain no more than 60% of total variance during  
304 the 2016 and 2019/20 QBO disruptions (Anstey et al., 2021). As a result, the QBO variability can be, to  
305 a very good approximation, compactly depicted by the trajectory of  $(PC_1(t), PC_2(t))$  in a linear space  
306 spanned by the first two orthonormal EOFs.

307 As in previous studies (Wallace et al., 1993; Taguchi, 2010; Christiansen et al. 2016; Serva et al.  
308 2020; DallaSanta et al., 2021), the instantaneous amplitude ( $am$ ) and phase ( $\psi$ ) of the QBO are defined  
309 as

$$310 \quad am = \sqrt{PC_1^2 + PC_2^2} \quad (1)$$

$$311 \quad \psi = atan2(PC_2, PC_1) \quad (2)$$

312 Differentiating (2) with respect to time yields the instantaneous phase speed of the QBO:

$$313 \quad \psi' = (PC_1 \cdot PC_2' - PC_1' \cdot PC_2) / (PC_1^2 + PC_2^2) \quad (3)$$

314 Using Eqs. (1) – (3) and the monthly processed FUB data from 1953 to 2008, Taguchi (2010)  
315 obtained 672 months of  $am$  and  $\psi'$  and partitioned each time series of  $\{am\}$  and  $\{\psi'\}$  into 16 categories.  
316 The 16 categories correspond to the 16 combinations of four QBO phase quadrants at the 50-hPa level  
317 and four seasons. Using a bootstrap (Chernick, 2007) method, Taguchi (2010) seminally illuminated the  
318 annual synchronization of the QBO. Taguchi (2010) further used the bootstrap method to show that the

319 QBO signals during El Niño episodes exhibit weaker amplitude in six out of 16 categories and faster  
320 phase propagation in eight out of 16 categories at a 90% or 95% confidence level (refer to Figure 6 in  
321 Taguchi, 2010).

322 It is worth pointing out that while Taguchi’s conclusion is physically meaningful, his statistical  
323 analysis is not robust concerning the ENSO influence on the QBO. For instance, there are 18 sample  
324 points in the (MAM, E) category where MAM stands for the months of boreal spring, i.e., March, April,  
325 and May while E indicates the QBO winds at the 50-hPa level are easterly. As Taguchi (2010) mentioned  
326 that the actual sample size should be six rather than 18 due to the data clustering. Among those 18 months  
327 of data, there are six for El Niño conditions and one for La Niña condition. Also pointed out by Taguchi  
328 (2010), actually sample sizes are two and one for El Niño and La Niña conditions, respectively, in the  
329 (MAM, E) category. It is hard to imagine we can infer any meaningful result from one La Niña sample  
330 point and two El Niño sample points out of the sample with its size being nine because Chernick (2007)  
331 points out that samples of size less than 10 are usually too small to rely on sample estimates, even in  
332 “nice” parametric cases, and that we should expect that such sample sizes are also too small for bootstrap  
333 estimates to be of much use (see his page 174). With regard to the above-mentioned (MAM, E) category,  
334 the following conclusion is evidently not robust: the QBO amplitude during El Niño episodes is weaker  
335 than that during La Niña episodes at a 95% confidence level (refer to Figure 6(b) in Taguchi, 2010)  
336 because one extreme La Niña and/or a couple of extreme El Niño sample points can influence the  
337 outcome of the statistical test.

338 Since we have observed 21 El Niño and 15 La Niña events between 1953 and 2015, the sample sizes  
339 of El Niño and La Niña appear large enough for us to conduct a classical parametric test. Namely, we  
340 have two sample spaces: one consists of 21 independent El Niño events and the other contains 15  
341 independent La Niña events. For each ENSO event, we define the amplitude  $[am]$  and phase speed  $[\psi']$

Deleted: (A)

Deleted: ( $\Psi'$ )

344 of the QBO as the monthly  $am$  in Eq. (1) and the monthly  $\psi'$  in Eq. (3) that are averaged over the number  
 345 of months of that event. Thus, two random variables  $[am]$  and  $[\psi']$ , i.e., the mean amplitude and mean  
 346 phase speed of the QBO during an ENSO episode, are defined both on the El Niño sample space and on  
 347 the La Niña sample space. Note that in this paper, a quantity enclosed by a pair of square brackets denotes  
 348 the average value of that quantity over the duration (i.e., the total number of months) of an ENSO event.

349 We employ Welch's  $t$ -test (Moser and Stevens, 1992) to examine whether there is a significant  
 350 difference in  $[am]$  or  $[\psi']$  between the El Niño and La Niña population means. For the sake of  
 351 conciseness, we will refer to  $[am]$  and  $[\psi']$  as  $A$  and  $\Psi'$ , respectively, in this subsection and section 3.

352 To examine whether the sample mean QBO amplitude is significantly different between El Niño and  
 353 La Niña, we first construct the statistic:

$$354 \quad t = \frac{A_1 - A_2}{s_{A_1 - A_2}} \quad (4)$$

355 where  $A_1$  and  $A_2$  are the values of  $A$ s that are averaged over the number of the El Niño and La Niña  
 356 events, respectively.

$$357 \quad s_{A_1 - A_2} = \sqrt{\frac{s_{A_1}^2}{N_1} + \frac{s_{A_2}^2}{N_2}} \quad (5)$$

358 where  $s_{A_1}$  and  $s_{A_2}$  are the corrected sample standard deviation of  $A$  for El Niño and La Niña,  
 359 respectively while  $N_1$  and  $N_2$  are the sample sizes of El Niño and La Niña events. According to Moser  
 360 and Stevens (1992), the degrees of freedom for the  $t$ -distribution is

$$361 \quad \nu = \frac{\left(\frac{s_{A_1}^2}{N_1} + \frac{s_{A_2}^2}{N_2}\right)^2}{\left(\frac{s_{A_1}^2}{N_1}\right) / (N_1 - 1) + \left(\frac{s_{A_2}^2}{N_2}\right) / (N_2 - 1)} \quad (6)$$

### 362 2.3.3 Analysis of the QBO forcings

Deleted: A

Deleted:  $\Psi'$

Deleted: A

Deleted:  $\Psi'$

367 The QBO owes its existence to wave-mean flow interaction (Lindzen and Holton, 1968; Holton and  
 368 Lindzen, 1972; Plumb, 1977). The evolution of zonal mean zonal winds is governed by the transformed-  
 369 Eulerian-mean (TEM) momentum equation formulated in pressure coordinates on a sphere (Andrews et  
 370 al., 1983):

$$371 \quad \frac{\partial \bar{u}}{\partial t} = \bar{G} + \frac{1}{\rho_0 a \cos \varphi} \nabla \cdot \mathbf{F} - \left\{ \frac{\bar{v}^*}{a \cos \varphi} \left[ \frac{\partial}{\partial \varphi} (\bar{u} \cos \varphi) - f \right] + \bar{\omega}^* \frac{\partial \bar{u}}{\partial p} \right\} + \bar{X}, \quad (7)$$

372 where the Eliassen-Palm flux  $\mathbf{F}$  is defined as

$$373 \quad \mathbf{F} = \{F^{(\varphi)}, F^{(p)}\} = a \cos \varphi \{-\overline{u'v'} + \psi \bar{u}_p, -\overline{u'\omega'} - \varepsilon [(a \cos \varphi)^{-1} (\bar{u} \cos \varphi)_\varphi - f]\}, \quad (8)$$

374 and its divergence as

$$375 \quad \nabla \cdot \mathbf{F} = \frac{1}{a \cos \varphi} \frac{\partial}{\partial \varphi} (F^{(\varphi)} \cos \varphi) + \frac{\partial F^{(p)}}{\partial p}. \quad (9)$$

376 In Eq. (7),  $t$  denotes time,  $p$  pressure,  $\varphi$  latitude,  $(u, v, \omega)$  "velocity" in (longitude, latitude, pressure)  
 377 coordinates,  $a$  the mean radius of Earth,  $\rho_0$  pressure-dependent basic density, and  $f$  the Coriolis  
 378 parameter. In Eq. (8),  $\varepsilon$  is defined as

$$379 \quad \varepsilon = \overline{v'\theta'}/\bar{\theta}_p = -\overline{v'T'}/\left(\frac{\kappa \bar{T}}{p} - \frac{\partial \bar{T}}{\partial p}\right), \quad (10)$$

380 where  $\theta$  denotes potential temperature,  $T$  temperature, and  $\kappa$  the ratio of the gas constant to the specific  
 381 heat at constant pressure. Note that in Eqs. (7) – (10) primes denote departures from the zonal means  
 382 which are represented by overbars, and residual meridional and vertical velocities, i.e.,  $\bar{v}^*$  and  $\bar{\omega}^*$ , are  
 383 defined as  $(\bar{v} - \frac{\partial \psi}{\partial p})$  and  $(\bar{\omega} + \frac{1}{a \cos \varphi} \frac{\partial (\varepsilon \cos \varphi)}{\partial \varphi})$ , respectively.

384 On the right hand side (RHS) of Eq. (7), the first term,  $\bar{G}$ , is the forcing from the GWs parameterized  
 385 in E2.2 models; the second term,  $\frac{1}{\rho_0 a \cos \varphi} \nabla \cdot \mathbf{F}$ , is the forcing driven by the waves resolved by GISS  
 386 E2.2 models; the third term,  $-\left\{ \frac{\bar{v}^*}{a \cos \varphi} \left[ \frac{\partial}{\partial \varphi} (\bar{u} \cos \varphi) - f \right] + \bar{\omega}^* \frac{\partial \bar{u}}{\partial p} \right\}$ , is associated with the TEM



387 advection; and last term,  $\bar{X}$ , is the zonal component of friction or other nonconservative mechanical  
388 forcing (Andrews et al., 1987). Since  $\bar{X}$  is small as far as the QBO is concerned, we will focus on  
389 analyzing the first three terms of Eq. (7) and ignore the last term of that equation in this study.

390

### 391 **3. Revisiting the ENSO modulation of the QBO from observations**

392 In the era of big data, bootstrap methods are a powerful tool that is used to analyze uncertainties for  
393 any machine learning model. However, the bootstrap methods cannot get something for nothing. It is  
394 not reliable if sample size is too small. In this section, we will use the classical parametric method  
395 outlined in subsection 2.3.2 to revisit the ENSO modulation of the QBO using the FUB data described  
396 in subsection 2.1.

397 The solid and dashed black lines in Fig. 1 depicts the two leading EOFs derived from the monthly  
398 anomalies of the FUB zonal winds between 1953 and 2015. The vertical structures of those two EOFs  
399 are very similar to those depicted in Fig. 2a of Taguchi (2010) who used the FUB zonal winds from 1953  
400 to 2008. Our calculated two leading EOFs account for 92.6% of the vertical structure variance (57.1%  
401 by EOF1 and 35.5% by EOF2) which is slightly smaller than the value of 96.1% shown in Taguchi  
402 (2010). Note that this discrepancy is not mainly due to the difference in the adopted time spans. When  
403 we use the monthly anomalies of the FUB zonal winds between 1953 and 2008, the resultant two leading  
404 EOFs account for 92.9% of the vertical structure variance (57.0% by EOF1 and 35.9% by EOF2). Coy  
405 et al. (2020) pointed out that the descent of the QBO winds varies at intraseasonal, seasonal, and  
406 interannual time scales (see their Figure 1 for more details). Thus, it is natural that two leading EOFs  
407 explain more variance of the FUB zonal winds when those winds have been deseasonalized and  
408 subjected to a 5-month running averaging.

409 As mentioned before, there are 21 El Niño and 15 La Niña episodes between 1953 and 2015, i.e.,  
410  $N_1 = 21$  and  $N_2 = 15$ . Our calculations yield  $A_1 = 39.5 \text{ ms}^{-1}$ ,  $A_2 = 42.4 \text{ ms}^{-1}$ ,  $\nu = 33$ , and  $t =$   
411  $-1.50$ . Apparently,  $A_1 < A_2$ , which suggests that the QBO amplitude is smaller during El Niño than  
412 during La Niña. Performing a two-tailed test, however, we find that the QBO amplitudes during El Niño  
413 episodes are not statistically different from those during La Niña episodes at the 5% significance level.

Deleted: 10%

414 This is consistent with the finding of the observational study by Yuan et al. (2014), namely, the ENSO  
415 modulation of the QBO amplitude is less robust than that of the QBO period. This is also consistent with  
416 the findings of the modeling studies conducted by Schirber (2015) and Serva (2020).

417 Note that when we use the FUB zonal winds and the ERSSTv5 data over the 1953–2008 period as  
418 Taguchi (2010), our calculations yield  $N_1 = 19$ ,  $N_2 = 13$ ,  $A_1 = 39.1 \text{ ms}^{-1}$ ,  $A_2 = 43.1 \text{ ms}^{-1}$ ,  $\nu = 29$ ,  
419 and  $t = -1.98$ . A two-tailed test shows that the difference of the QBO amplitude between El Niño and  
420 La Niña is not statistically significant at the 5% significance level either.

421 Apparently, no matter whether we use the FUB data over the 1953–2008 period or over the 1953–  
422 2015 period, the influence of the ENSO on the QBO amplitude is not statistically significant at the 5%  
423 significance level. Thus, we will not further explore whether GISS E2.2 models can simulate the ENSO  
424 modulation of the QBO amplitude in this study.

425 To examine whether the sample mean QBO phase speed is significantly different between El Niño  
426 and La Niña, we similarly use Eqs. (4) – (6) except that  $A_1$  and  $A_2$  are replaced by  $\Psi_1^*$  and  $\Psi_2^*$ ,  
427 respectively. Based on the data from 1953 to 2015, we obtained  $N_1 = 21$  and  $N_2 = 15$ ,  $\Psi_1^* = 0.246$   
428 radians/month,  $\Psi_2^* = 0.183$  radians/month,  $\nu = 28$ , and  $t = 2.36$ . Evidently,  $\Psi_1^* > \Psi_2^*$ , indicating that  
429 the phase speed of the QBO is greater during El Niño than during La Niña. Performing a two-tailed test,  
430 we ascertain that the phase speed of QBO during El Niño episodes are statistically different from those  
431 during La Niña episodes at the 5% significance level. Put in another way, the mean QBO period of 25.6

433 months (i.e.,  $2\pi/0.246$ ) during El Niño is statistically shorter than that of 34.3 months (i.e.,  $2\pi/0.183$ )  
434 during La Niña over the 1953–2015 period. Furthermore, when we use the FUB zonal winds and the  
435 ERSSTv5 data over the 1953–2008 period as Taguchi (2010), our calculations yield  $N_1 = 19$  and  $N_2 =$   
436 13,  $\Psi_1^* = 0.253$  radians/month,  $\Psi_2^* = 0.180$  radians/month,  $\nu = 25$ , and  $t = 2.87$ . Apparently, we  
437 reach a similar conclusion that the mean QBO period of 24.8 months (i.e.,  $2\pi/0.253$ ) during El Niño is  
438 statistically shorter than that of 34.9 months (i.e.,  $2\pi/0.180$ ) during La Niña at the 5% significance level.

439 Thus, no matter whether we use the FUB data over the 1953–2008 period or over the 1953–2015  
440 period, the influence of the ENSO on the QBO phase speed is statistically significant at the 5%  
441 significance level. In other words, our observational study robustly buttresses the following conclusion  
442 of Taguchi (2010): the QBO descent is faster during El Niño than during La Niña. Henceforth, we will  
443 focus only on the ENSO modulation of the QBO period in this study.

444 To facilitate comparison with other studies (e.g., Taguchi, 2010; Christiansen et al., 2016; Serva et  
445 al. 2020), we also calculate the mean phase speed of the QBO by averaging monthly  $\psi'$  in Eq. (3) over  
446 all the 210 months of the El Niño episodes and over all the 201 months of the La Niña episodes between  
447 1953 and 2015. Subsequently, we obtain the mean QBO period of 25.6 months during El Niño and of  
448 32.2 months during La Niña for the 1953–2015 period. Similarly, we obtain the mean phase speed of the  
449 QBO by averaging monthly  $\psi'$  in Eq. (3) over all the 186 months of the El Niño episodes and over all  
450 the 174 months of the La Niña episodes for the 1953–2008 period. The resultant values are 24.9 and 32.2  
451 months, respectively, which are very close to 25 and 32 months inferred by Taguchi (2010). No matter  
452 whether the selected FUB data span from 1953 to 2008 or range from 1953 to 2015, we robustly conclude  
453 that the QBO descent rate is faster during El Niño than during La Niña.

454 Note that it is difficult to rigorously determine the degrees of freedom for a  $t$ -test when we choose the  
455 monthly data as sample points which share some common characteristics, i.e., are not independent of

456 each other during an ENSO event (for more details, refer to Taguchi, 2010). In the remainder of this  
457 paper, when we need to conduct a Welch's  $t$ -test we choose the QBO period averaged over each ENSO  
458 episode as a sample point. Otherwise, the mean values during El Niño or La Niña are referred to the  
459 quantities averaged over all the months of El Niño or La Niña category in alignment with previous works  
460 conducted by Taguchi (2010), Christiansen et al. (2016), and Serva et al. (2020).

461 The QBO is mainly driven by tropical waves (Lindzen and Holton, 1968; Holton and Lindzen, 1972;  
462 Plumb 1977) of which tropical convection is an important source (Holton, 1972; Salby and Garcia, 1987;  
463 Bergman and Salby, 1994; Tsuda et al., 2009; Alexander et al., 2017). To investigate how tropical  
464 convection is influenced by the ENSO, we first produce the monthly anomalies of OLR from NOAA  
465 NCEI over the 1979–2015 period. Then we obtain the mean OLR anomalies (OLRA) for La Niña and  
466 El Niño conditions by averaging the monthly OLRA over all the months that fall into La Niña and El  
467 Niño categories, respectively. Fig. 2a show that mean OLRA exhibit a broad and positive pattern that  
468 spans the central and eastern equatorial Pacific and a negative pattern in the maritime continent for the  
469 La Niña conditions. In contrast, Fig. 2b show that they exhibit a broad and negative pattern that spans  
470 the central and eastern equatorial Pacific and a positive pattern in the maritime continent for the El Niño  
471 conditions. The large differences in the mean OLRA in Fig. 2c between El Niño and La Niña conditions  
472 are closely related with the contrast in the SSTA patterns shown in Fig. 3. Namely, the distinctive  
473 patterns of positive and negative SSTA extend over the central and eastern Pacific during the El Niño  
474 and La Niña episodes, respectively, which not only gives rise to the corresponding positive and negative  
475 rainfall anomalies (Philander, 1990) and the concomitant OLRA shown in Fig. 2, but also leads to  
476 various teleconnections outside the tropics (Domeisen et al., 2019).

477 In order to test whether the difference patterns of OLRA and SSTA shown in Figs. 2c and 3c are  
478 statistically robust we use [OLRA] and [SSTA] as our sample points to perform two-tailed tests. Figs.

Deleted: OLR anomalies

Deleted: OLR anomalies

Deleted: OLR anomalies

Deleted: SST anomalies

Deleted: SST anomalies

Deleted: OLR anomalies

485 [S1 and S2 shown in the supplement demonstrate that the difference patterns are statistically significant](#)  
486 [at the 5% significance level.](#)

487 In the next section, we will evaluate how the ENSO modulates the QBO periods in the E2.2 models  
488 and whether those models can realistically capture the contrast in the OLR (and convection) patterns that  
489 generally underlies the difference in wave driving of the QBO between warm and cold ENSO conditions.

490

#### 491 **4. ENSO modulation of the QBO period in GISS E2.2 models**

492 Now we investigate the ENSO modulation of the QBO period in the ensemble simulations listed in  
493 Table 1.

494 We first calculate the monthly mean anomalies of zonal winds using the method outlined in  
495 subsection 2.3.1. Then we average those monthly mean anomalous zonal winds over the latitudinal belt  
496 from 5° S to 5° N to obtain the monthly QBO winds over the 1871 to 2013 period at the following seven  
497 pressure levels: 70, 50, 40, 30, 20, 15, and 10 hPa.

498 As in section 3, we decompose the QBO winds from 10 to 70 hPa over the 1871–2013 period into  
499 two leading pairs of empirical orthogonal functions (EOFs) and principal components (PCs). For each  
500 of the 19 ensemble simulations listed in Table 1, the first two leading EOFs account for at least 92.9%  
501 of the vertical structure variance which is comparable to the value derived from the observations  
502 discussed in section 3. Since coupled models encounter more difficulties in simulating the ENSO  
503 modulations of the QBO (Serva et al. 2020, see their Fig.4 for more details), we first look into the  
504 ensemble simulations from the Coupled–NINT–AP model, which incorporates the most up-to-date cloud  
505 parameterization schemes. The red and blue lines in Fig. 1 depicts the first two leading EOFs from each  
506 of all five Coupled–NINT–AP runs. For each of those five runs, the first two leading EOFs account for  
507 at least 93.8% of the vertical structure variance. The vertical structures of those two EOFs from each

508 Coupled–NINT–AP run are broadly similar to the solid and dashed black lines derived from observations  
509 in Fig. 1. The respective vertical structures of the first two leading EOFs are almost identical among all  
510 five Coupled–NINT–AP ensemble runs, which is expected because all runs share the same model and  
511 differ from each other only in their initial conditions. It is worth noting that the vertical structures of the  
512 first two leading EOFs simulated by Coupled–NINT–AP are somewhat different from those observed  
513 below the 20 hPa level because none of CMIP models could simulate a QBO in the lower stratosphere  
514 that is as strong as the observed (Richter et al., 2020). In addition, we find that the vertical structures of  
515 the first two leading EOFs from other three ensemble simulations listed in Table 1 (figures not shown)  
516 are comparable to those from the Coupled–NINT–AP runs. ▼

517 For the ensemble simulations listed in Table 1, we define an El Niño or La Niña event according to  
518 the criterion described in subsection 2.3.1. Similarly, Eq. (3) is used to calculate the instantaneous (i.e.,  
519 monthly) phase speed of the simulated QBO. For each El Niño or La Niña event, the mean phase speed  
520 of the simulated QBO from any individual run listed in Table 1 is obtained by averaging the  
521 instantaneous phase speeds of the simulated QBO over the number of months of that event. Accordingly,  
522 we have one sample space consisting of independent El Niño events and the other consisting of  
523 independent La Niña events. In addition, we employ a two-tailed Welch's  $t$ -test outlined in subsection  
524 2.3.2 to examine whether there is a significant difference in the phase speed of the simulated QBO  
525 between the El Niño and La Niña population means.

526 Table 2 describes how the ENSO influence the QBO period in each member of all ensembles, where  
527 E[1-4] represent AMIP–OMA–SP, AMIP–OMA–AP, Coupled–NINT–SP, and Coupled–NINT–AP  
528 ensembles, respectively while  $r_1, r_2, \dots$  indicate its respective member of each ensemble. As we  
529 mentioned in subsection 2.3.1, for the member  $r_1$  of E1, i.e., the first run of the AMIP–OMA–SP  
530 ensemble, there are 34 El Niño and 30 La Niña events between 1871 and 2013, i.e.,  $N_1 = 34$  and  $N_2 =$

**Deleted:** Thus, the simulated QBO variabilities in each ensemble can be, to a very good approximation, compactly depicted by the trajectory of  $(PC_1(t), PC_2(t))$  in a linear space spanned by the first two orthonormal EOFs.

535 30 in Eqs. (5) and (6). Then we obtained the phase speed of the QBO for each episode of those 34 El  
536 Niño and 30 La Niña events, from which we derived the mean phase speed of the QBO averaged over  
537 the 34 El Niño and 30 La Niña events, respectively. Accordingly, our mean phase speeds of the QBO  
538 simulated by r1 of E1 averaged over the El Niño and La Niña events are obtained as 0.202 radians/month  
539 and 0.185 radians/month, respectively, and the standard deviations about those mean phase speeds as  
540 0.0345 radians/month and 0.0275 radians/month, respectively. Substituting those numbers into  
541 Eqs. (4) – (6) yields  $\nu = 61$ , and  $t = 2.25$ . Therefore, the phase speed of the QBO simulated by r1 of  
542 E1 is statistically significantly greater during El Niño than during La Niña at the 5% significance level.  
543 Accordingly, we register the mean QBO period of 31.1 months (i.e.,  $2\pi/0.202$ ) during the El Niño  
544 episodes and 34.0 months (i.e.,  $2\pi/0.185$ ) during the La Niña episodes as the entries for r1 of E1 in  
545 Table 2. Since the phase speeds of the QBO simulated by r1 of E1 are statistically significantly different  
546 between the El Niño and La Niña categories at the 5% significance level, we can regard the QBO periods  
547 as being statistically significantly different between El Niño and La Niña episodes and register their  
548 difference, -2.9 months, in Table 2 with a pair of parentheses indicating this significance. Similarly, we  
549 calculated the QBO periods during ENSO extremes and their difference simulated by every member of  
550 all ensembles and registered them in Table 2 where the numbers in the parentheses indicate that the  
551 phase speed of the simulated QBO is statistically significantly greater during El Niño than during La  
552 Niña at the 5% significance level.

553 Table 2 shows that 18 of 19 runs from the four GISS E2.2 models listed in Table 1 can simulate the  
554 ENSO modulation of the QBO period discussed in section 3. For each Coupled–NINT–AP ensemble  
555 run, the phase speed of the simulated QBO is statistically significantly greater during El Niño than during  
556 La Niña at the 5% significance level. For the AMIP–OMA–SP and AMIP–OMA–AP ensembles, most  
557 members also generate a spontaneous QBO whose phase speed is statistically significantly greater during

558 El Niño than during La Niña at the 5% significance level. Intriguingly, in none of the Coupled–NINT–  
559 SP ensemble runs is the phase speed of the simulated QBO statistically significantly different between  
560 El Niño and La Niña episodes at the 5% significance level albeit the contrast in the QBO periods between  
561 the two categories simulated by r1 of E3 (i.e., Coupled–NINT–SP) is equal to -6.2 months and greater  
562 than that simulated by most members of Coupled–NINT–AP. We will look further into this issue in  
563 section 6.

## 564 5. Mechanisms of the ENSO modulation of the QBO period in GISS E2.2 models

### 565 5.1 ENSO modulation of the QBO forcings

566 Section 4 shows that the ENSO modulation of the QBO period can be simulated by each of the AMIP–  
567 OMA–SP, AMIP–OMA–AP, and Coupled–NINT–AP models. The difference in the phase speed of the  
568 simulated QBO between ENSO extremes is statistically significant at the 5% significance level for most  
569 of those model runs. For Coupled–NINT–SP, one of its historical runs exhibits an opposite response,  
570 namely, the simulated QBO propagates downward slower during El Niño than during La Niña while  
571 other four runs from the identical model configuration do bring about a faster phase speed of the QBO  
572 during warm ENSO events. However, no matter whether the difference in the QBO period simulated by  
573 Coupled–NINT–SP is positive or negative between ENSO extremes, it is not statistically significant at  
574 the 5% significance level. In this section, we start with investigating how the first three terms in Eq. (7),  
575 i.e., the parameterized GW forcing, the resolved wave forcing, and the TEM advection, respond to ENSO  
576 extremes and how their evolutions are related with those of the simulated QBO winds.

Deleted: simulated by the GISS E2.2 models

577 As shown in sections 3 and 4, both the observed and simulated QBO can be very well represented by  
578 the trajectory of  $(PC_1(t), PC_2(t))$  in a linear space spanned by the first two orthonormal EOFs. In other  
579 words, at any time  $t$ , the QBO wind profile,  $U'_{profile}$  is very close to the following linear combination:  
580  $PC_1(t) \cdot EOF_1 + PC_2(t) \cdot EOF_2$ . Here, the QBO wind,  $U'$ , refers to the deseasonalized and smoothed



582 monthly mean zonal winds averaged over the zonal belt from 5° S to 5° N. We construct the composite  
583 fields of the QBO winds, the GW forcing, the resolved wave forcing, and the TEM advection according  
584 to the phase angle of the QBO wind profiles. For each month that falls into the El Niño or La Niña  
585 category, we use Eq. (2) to calculate the phase angle of the QBO wind profile, each cycle of which over  
586 the 1871–2013 period is divided into 24 bins with the bin size of 15°. Note that if two QBO wind profiles  
587 belong in the same bin, they look similar because any one of them can be approximated by the other  
588 multiplied by a scalar factor. Therefore, for each of the El Niño and La Niña categories, it is very natural  
589 for us to generate the composite QBO winds for that category by averaging all wind profiles in each bin  
590 and produce the concomitant composite fields of the GW forcing, the resolved wave forcing, and the  
591 TEM advection in the corresponding bin.

592 Fig. 4 depicts the composite fields of the QBO winds (black contours) and parameterized (left panels)  
593 and resolved (right panels) wave forcing averaged over all realizations of the Coupled–NINT–AP  
594 ensemble. All composite fields in this section have been subjected to the averaging over the latitudinal  
595 belt from 5°S to 5°N. The ensemble average is achieved on the basis that the respective vertical  
596 structures of the first two leading EOFs are almost identical among all five Coupled–NINT–AP ensemble  
597 runs as demonstrated in Fig. 1. Both Figs. 4a and 4b show a characteristic feature of the QBO. Namely,  
598 the maximum eastward and westward wave forcing from parameterized GWs are located below and  
599 propagate downward with the westerly and easterly QBO jets. Fig. 4c reveals the stronger parameterized  
600 GW forcing in both eastward and westward shear zones of the QBO winds during El Niño than during  
601 La Niña, which gives rise to the faster phase speed of the QBO during warm ENSO episodes than during  
602 its cold counterparts. Figs. 4d and 4e show that the relationship between resolved wave forcing and the  
603 QBO winds are somewhat more complex. When zonal wind anomalies are close to zero, the coherent  
604 and modest resolved westward wave forcing helps the easterly shear zone of the QBO winds to propagate

Deleted: expressed

Deleted: also

607 downwards from the 10 hPa level to the 70 hPa level during both the cold and warm ENSO episodes  
608 while the coherent and modest resolved eastward wave forcing helps the westerly shear zone of the QBO  
609 winds to propagate downwards only from the 20 hPa level to the 70 hPa level during both the cold and  
610 warm ENSO episodes. At altitudes above the 20 hPa level, easterly jet cores are modestly weakened by  
611 the resolved eastward wave forcing during the two extreme ENSO phases. In particular, Fig. 4f indicates  
612 that at altitudes above the 30 hPa level the response of the resolved wave forcing to the ENSO acts to  
613 slow down the downward propagation of the QBO during El Niño than during La Niña. However, the  
614 parameterized GW forcing shown in Fig. 4 clearly dominates over the resolved wave forcing, which is  
615 consistent with the finding of DallaSanta et al. (2021) that the parameterized convective GWs play a  
616 dominant role in generating the spontaneous QBO in the GISS E2.2 models.

617 Figs. 5a–5c depict the composite fields of the QBO winds (black contours) and TEM advection  
618 averaged over all realizations of the Coupled–NINT–AP ensemble. Comparing Figs. 5a–5c with Fig. 4  
619 reveals that the TEM advection composite is also larger than composite resolved wave forcing in the  
620 Coupled–NINT–AP model. Thus, the QBO simulated by this model is intimately related to the  
621 parameterized GW forcing and the TEM advection. It is well-known that while wave forcing is largely  
622 balanced out by the TEM advection in the extratropical stratosphere (Haynes, et al., 1991) tropical wave  
623 forcing not only drives internal variabilities of zonal winds but also cancel out the TEM advection in the  
624 stratosphere (Scott and Haynes, 1998). Figs. 5a–5b also show that the maximum positive and negative  
625 advective tendencies are located above rather than below and propagate downward with the westerly and  
626 easterly QBO jets, thus acting to slow down the downward propagation of the QBO, which is mainly  
627 caused by the persistent tropical upwelling and a general feature of the QBO (Giorgetta et al. 2006; Rind  
628 et al., 2014). Fig. 5c indicates that there exist stronger positive and negative advective tendencies above  
629 the westerly and easterly QBO jets during El Niño than during La Niña. In other words, the TEM

630 advection alone leads to a slower phase speed of the QBO during El Niño than during La Niña. This is  
631 not surprising because El Niño gives rise to a stronger tropical upwelling in the lower stratosphere (Calvo  
632 et al., 2010; Simpson et al., 2011; Domeisen et al., 2019).

633 Figs. 5d–5f show the composite QBO winds (black contours) and the composite sum of parameterized  
634 GW forcing, resolved wave forcing, and TEM advection averaged over all realizations of the Coupled–  
635 NINT–AP ensemble. In other words, the upper, middle, and lower panels depict the sum of the fields  
636 shown in all the corresponding panels of Fig. 4 and Figs. 5a–5c. The pattern of the composite sum is  
637 generally determined by the pattern of parameterized GW forcing even though the latter is more coherent  
638 than the former. Thus, we conclude that the shorter QBO period during El Niño simulated by Coupled–  
639 NINT–AP is mainly caused by stronger parameterized GW forcing during warm ENSO episodes. We  
640 also find that stronger parameterized GW forcing during warm ENSO events are simulated by AMIP–  
641 OMA–SP and AMIP–OMA–AP models (figures not shown), which helps us understand why most  
642 members from each of those three ensembles generate a spontaneous QBO whose phase speed is  
643 statistically significantly greater during El Niño than during La Niña at the 5% significance level.

644 Now we explore how ENSO influences parameterized GW forcing, resolved wave forcing, and TEM  
645 advection simulated by the Coupled–NINT–SP model, i.e., the remaining model listed in Tables 1 and  
646 2. Contrasting between Fig. 6a and Fig. 4c reveals that the ensemble mean composite response to the  
647 ENSO of parameterized GW forcing simulated by Coupled–NINT–SP is substantially weaker than that  
648 simulated by Coupled–NINT–AP. Although the Coupled–NINT–SP simulations still bring about  
649 enhanced westward parameterized GW forcing in the easterly shear zones of the simulated QBO winds  
650 during El Niño in contrast to La Niña, the magnitude of the reinforcement is only about two thirds of  
651 that simulated by Coupled–NINT–AP. In particular, in Fig. 6a there is no coherent pattern of enhanced  
652 eastward parameterized GW forcing in the westerly shear zones of the QBO winds simulated by

Deleted: Figure 5

654 Coupled–NINT–SP, which is in glaring contrast to the coherent pattern of positive enhancement shown  
655 in Fig. 4c generated from the Coupled–NINT–AP ensemble. Figs. 6b and 6c show that both resolved  
656 wave forcing and TEM advection respond to the ENSO weakly and uniformly in the Coupled–NINT–  
657 SP ensemble simulations. Combining all three composite fields together, Fig. 6d demonstrates that the  
658 ensemble mean of the Coupled–NINT–SP simulations still simulates a coherent but much weaker  
659 response to the ENSO of resultant forcing at altitudes above the 40 hPa level, which helps us to explain  
660 why only some of the Coupled–NINT–SP ensemble runs can simulate a faster QBO descent rate during  
661 El Niño than during La Niña and the ENSO does not make a difference in the phase speed of the QBO  
662 that is statistically significant at the 5% significance level in any of those Coupled–NINT–SP runs.

## 663 5.2 ENSO modulation of the generation and propagation of parameterized gravity waves

664 A natural question that arises is how the parameterized GW forcing relates to the SSTA of ENSO  
665 extremes specified in or simulated by the GISS E2.2 models listed in Table 1. Figs. 7a and 7b show the  
666 ensemble averages of the composite SSTA averaged over all La Niña and El Niño months respectively  
667 over the 1871–2013 period simulated by Coupled–NINT–AP. Comparing Figs. 7a and 7b with Figs. 3a  
668 and 3b reveals that the amplitude of the ENSO simulated by Coupled–NINT–AP is larger than the  
669 observed. Figs. 7c and 7d show the differences between the simulated SSTA arising from the ENSO  
670 events shown in Figs. 7a and 7b and the observed SSTA, shown in Figs. 3a and 3b, indicating that the  
671 largest discrepancies occur over the western and eastern equatorial Pacific. Figs. 7a and 7b also  
672 demonstrate that the model has a capability to simulate the ENSO amplitude asymmetry (Cane and  
673 Zebiak, 1987; Yu and Mechoso, 2001), namely, the amplitudes of the ENSO are relatively larger during  
674 warm episodes than during cold episodes. As in Fig. 3 of Zhao and Sun (2022), Fig. 7e depicts the sum  
675 of the composite SSTA shown in Figs. 7a and 7b that they used to characterize the ENSO amplitude  
676 asymmetry while Fig. 7f shows their difference. Their Fig. 3 reveals that most CMIP6 models cannot

Deleted: SST anomalies

Deleted: SST anomalies

Deleted: that

Deleted: SST anomalies

Deleted: ones

Deleted: SST anomalies

683 simulate the pattern of a positive residual in the sum of the composites of ENSO extremes in the tropical  
684 eastern Pacific. Further comparison between Fig. 3 in Zhao and Sun (2022) and Fig. 7e indicates that the  
685 ENSO amplitude asymmetry simulated by Coupled-NINT-AP is only about 50% of that simulated by  
686 the GISS-E2-1-H model discussed in their study whose ENSO amplitude asymmetry is comparable to  
687 the observed.

688 Since this study is chiefly concerned with the ENSO modulation of the QBO period, we focus on the  
689 ensemble mean difference between the composite ~~SSTA~~ of ENSO extremes, which can be interpreted  
690 as the trough-to-crest amplitude of the ENSO cycle. Comparing Fig. 8a with Fig. 3c indicates that the  
691 trough-to-crest ENSO amplitude derived from the HadISST1 dataset over the 1871–2013 period is  
692 somewhat smaller than that derived from the ERSSTv5 dataset over the 1953–2015 period, which is  
693 consistent with the finding by Grothe et al. (2019) that the increase in the ENSO variability is statistically  
694 significant (>95% confidence) from the preindustrial to recent era, no matter whether the latter is defined  
695 by the previous 30, 50, 75, or 100 years before 2016. Fig. 7f and Fig. 8 also reveal that the ENSO  
696 amplitude simulated by Coupled-NINT-AP is substantially greater than that simulated by Coupled-  
697 NINT-SP, which was previously revealed in Rind et al. (2020). The tendency to generate stronger ENSO  
698 oscillations means that the Coupled-NINT-AP runs will also more readily exceed the  $\pm 0.5^\circ\text{C}$  criteria  
699 for El Niño and La Niña events, and the Coupled-NINT-AP runs do simulate more ENSO events over  
700 the 1871–2013 period than the Coupled-NINT-SP runs as indicated in subsection 2.3.1. Fig. 8 further  
701 shows that the ENSO amplitude simulated by Coupled-NINT-SP is noticeably greater than ~~those~~  
702 specified in the AMIP-OMA-SP and AMIP-OMA-AP models (which, being derived from observations,  
703 are ~~identical~~) even though it is substantially weaker than that simulated by Coupled-NINT-AP.

Deleted: SST anomalies

Deleted: n

Deleted: n

Deleted: that

Deleted: the same

709 We also ascertain that the Hadley circulation simulated by each of the four models listed in Table 1  
710 strengthens and weakens during warm and cold ENSO episodes respectively (*figure not shown*), which  
711 is consistent with the finding by Oort and Yienger (1996).

712 Schirber (2015) discovered that the parameterized GW mean momentum source is about 15% larger  
713 in the El Niño ensemble than in the La Niña ensemble because the El Niño leads to enhanced  
714 precipitation and convective heating. Similarly, we calculate the absolute value of convective  
715 momentum fluxes (ACMF) at the source altitude and composite the ACMF anomalies averaged over the  
716 latitudinal belt between 5°S and 5°N from El Niño and La Niña categories respectively over the 1871–  
717 2013 period. Fig. 9 shows the composite difference in the equatorial mean ACMF anomalies between El  
718 Niño and La Niña over the 1871–2013 period, indicating that the absolute momentum fluxes at the source  
719 levels over the equatorial *belt* is larger during El Niño episodes than during La Niña episodes for each  
720 of 19 runs listed in Table 1. This finding is consistent with that of Geller et al. (2016b), Alexander et al.  
721 (2017), and Kang et al. (2018), namely, both convective GW momentum fluxes and convective GW  
722 wave forcing are generally stronger during El Niño than during La Niña in the equatorial region. The  
723 ensemble mean difference in the absolute momentum fluxes at the source levels averaged over that  
724 equatorial belt between El Niño and La Niña is obtained as 0.07, 0.15, 0.10, and 0.12 mPa for AMIP–  
725 OMA–SP, AMIP–OMA–AP, Coupled–NINT–SP, and Coupled–NINT–AP, respectively. Note that  
726 these composite differences in ACMF between El Niño and La Niña translate into ACMF being about  
727 10–20% larger in the El Niño ensembles than in the La Niña ensembles, thus agree with the Schirber  
728 (2015). Since the QBO period is inversely dependent upon the momentum flux (Plumb, 1977), the  
729 differences in equatorial absolute momentum fluxes at the source altitude contribute to shortening and  
730 lengthening of the simulated QBO period during warm and cold ENSO phases, respectively.

**Deleted:** Consistent with the simulated ENSO amplitudes, the response of the Hadley circulation to ENSO extremes simulated by Coupled–NINT–AP is substantially stronger than that simulated by Coupled–NINT–SP, which is in turn stronger than the those from two AMIP models whose responses to ENSO extremes are comparable (figures not shown)....

**Deleted:** best

739 Fig. 3 shows that the locations of warmest SSTs shift from the maritime continent during La Niña  
740 episodes to the central and eastern equatorial Pacific during El Niño episodes. Since strong convective  
741 activities over tropical oceans are generally located above the regions where the SSTs exceed 26°–28° C  
742 (Graham and Barnett, 1987; Zhang, 1993), strong convective activities also shift eastward from cold to  
743 warm ENSO phases, as illustrated in Fig. 2. Using satellite data, the climatological study by Sullivan et  
744 al. (2019) demonstrated that the occurrence of organized deep convection during El Niño events  
745 increases threefold in the central and eastern Pacific and decreases twofold outside of these regions in  
746 contrast to that during La Niña events. It is well-established that the Walker circulation strengthens  
747 during La Niña and weakens during El Niño (Bjerknes, 1969).

748 Next, we construct the equatorial zonal winds as the zonal winds averaged from 5°S to 5°N. Then we  
749 define the equatorial winds during La Niña and El Niño as the equatorial winds averaged over all months  
750 that fall into the La Niña and El Niño categories, respectively. Fig. 10 illuminates that the Walker  
751 circulation derived from ERA5 reanalysis during El Niño is substantially weaker than its counterpart  
752 during La Niña over the equatorial Pacific and the eastern equatorial Indian ocean. Particularly in the  
753 upper equatorial troposphere, the westerlies above the central and eastern Pacific during El Niño  
754 episodes are decreased by more than 50% as compared with those during La Niña ones while the  
755 easterlies above the equatorial Indian ocean and the maritime continent during El Niño conditions are  
756 weakened by more than 30% as compared with those during La Niña ones. Kawatani et al. (2019) argue  
757 that the weaker upper tropospheric winds during El Niño episodes enable a greater amount of GW  
758 momentum fluxes to be transferred from the troposphere into stratosphere because less GWs are filtered  
759 out. This argument assumes critical-level absorption of otherwise weakly damped, vertically propagating  
760 GWs, which was adopted by Lindzen and Holton (1968). The weaker Walker circulation leads to a

761 shorter QBO period during El Niño while the stronger Walker circulation results in a longer QBO period  
762 during La Niña.

763 Fig. 11 depicts the ensemble mean composite difference in the equatorial zonal wind anomalies  
764 between warm and cold ENSO extremes simulated by the E2.2 models listed in Table 1. The patterns of  
765 the simulated wind anomalies shown in Fig. 11 are very similar to that derived from the ERA5 reanalysis  
766 shown in Fig. 10c. Namely, the weakened Walker circulation simulated by the E2.2 models during El  
767 Niño episodes results in weaker upper tropospheric westerlies over the central and eastern equatorial  
768 Pacific and weaker upper tropospheric easterlies over the maritime continent and equatorial Indian ocean  
769 while the intensified Walker circulation simulated by the E2.2 models during La Niña episodes leads to  
770 stronger upper tropospheric westerlies over the central and eastern equatorial Pacific and stronger upper  
771 tropospheric easterlies over the maritime continent and equatorial Indian ocean. The difference in the  
772 wind filtering of upward propagating GWs causes a greater transfer of GW momentum fluxes into the  
773 tropical stratosphere during El Niño episodes than during La Niña episodes, leading to a shorter QBO  
774 period during El Niño events than during La Niña events. Fig. 11 reveals that the maximum contrast in  
775 the upper tropospheric zonal winds between warm and cold ENSO extremes simulated by two AMIP  
776 models, i.e., AMIP-OMA-SP and AMIP-OMA-AP, reaches  $-13.1 \text{ ms}^{-1}$  and  $-12.1 \text{ ms}^{-1}$ , respectively,  
777 over the central and eastern equatorial Pacific, and attains  $6.6 \text{ ms}^{-1}$  and  $6.4 \text{ ms}^{-1}$ , respectively, over  
778 the maritime continent and equatorial Indian ocean. Those maximum contrasts are somewhat smaller  
779 than what is derived from the ERA5 reanalysis shown in Fig. 10, namely  $-15.0 \text{ ms}^{-1}$  over the central  
780 and eastern equatorial Pacific and  $7.8 \text{ ms}^{-1}$  over the maritime continent and equatorial Indian ocean.  
781 However, the maximum contrast in the upper-tropospheric zonal winds over the central and eastern  
782 equatorial Pacific between warm and cold ENSO extremes simulated by two coupled ocean-atmosphere  
783 models, i.e., Coupled-NINT-SP and Coupled-NINT-AP, only reaches  $-7.5 \text{ ms}^{-1}$  and  $-8.2 \text{ ms}^{-1}$ ,

Deleted: 11



785 respectively, thus is substantially smaller than that derived from the ERA5 reanalysis. Meanwhile, the  
786 maximum contrast in the upper-tropospheric zonal winds over the maritime continent and equatorial  
787 Indian ocean between warm and cold ENSO extremes simulated by those two coupled models, reaches  
788  $7.0 \text{ ms}^{-1}$  and  $10.3 \text{ ms}^{-1}$ , respectively, which is slightly smaller than and somewhat larger than the  
789 observed values, respectively.

790 ~~The~~ comparison of the observed and simulated changes in the Walker circulation between warm and  
791 cold ENSO extremes shown in Figs. 10 and 11 can ~~both~~ account for a shorter QBO period simulated by  
792 all GISS E2.2 models and ~~explain why the two AMIP models can better capture the ENSO modulation~~  
793 of the QBO period than the Coupled–NINT–SP model as indicated in Table 2. ~~However,~~ it can neither  
794 explain why the Coupled–NINT–AP model can capture the ENSO modulation of the QBO period as two  
795 AMIP models nor ~~illuminate why the coupled model with the altered physics (i.e., Coupled–NINT–AP)~~  
796 performs better than the coupled model with the standard physics (i.e., Coupled–NINT–SP). ~~Further,~~  
797 comparing the simulated SST changes between warm and cold ENSO extremes shown in Figs. 7 and 8  
798 hints that the unduly amplified ENSO in the coupled AP runs holds the key to those unsettled issues that  
799 is detailed as follows.

800 Using a large ensemble of multiple climate models, Serva et al. (2020) discovered that the AMIP  
801 historical runs generally better capture the ENSO modulation of the QBO period than the coupled ocean-  
802 atmosphere historical simulations. In particular, among a few coupled ocean-atmosphere models that do,  
803 to various extents, capture the ENSO modulation of the QBO period, the common feature is that each of  
804 them can largely simulate the observed OLR anomaly pattern shown in Fig. 2c albeit the magnitudes of  
805 those simulated ~~OLRA~~ from their historical runs are roughly 50% stronger than the observed (for more  
806 details, refer to their Fig. 8 in Serva et al., 2020). For the sake of comparison, we construct the ensemble

Deleted: While t

Deleted: he

Deleted: can also

Deleted: ,

Deleted: can

Deleted: However,

Deleted: further

Deleted: OLR anomalies

§15 mean composite difference in the OLRA between warm and cold ENSO extremes in the same way we  
816 constructed the ensemble mean composite difference in the zonal wind anomalies depicted in Fig. 11.

Deleted: OLR anomalies

§17 Figs. 12a and 12b show that the patterns of the OLRA simulated by AMIP-OMA-SP and AMIP-  
818 OMA-AP largely resemble the observed one shown in Fig. 2c. Although the pattern simulated by  
819 AMIP-OMA-AP matches better with the observed, the convective activities during El Niño episodes  
820 simulated by AMIP-OMA-SP and AMIP-OMA-AP are apparently inadequate over the region where  
821 the upper tropospheric westerlies weaken most conspicuously during warm ENSO extremes shown in  
822 Figs. 11a and 11b, respectively. Thus, although the contrast in the wind filtering of GWs between El  
823 Niño and La Niña episodes simulated by the two AMIP E2.2 models are comparable to the observed,  
824 the difference in the GW momentum flux transferred into the equatorial stratosphere between warm and  
§25 cold ENSO extremes may well be smaller than the observed with the correct SSTs. This partly explains  
826 why the contrast between the observed mean QBO period during El Niño episodes (i.e., 25.6 months)  
827 and the observed mean QBO period during La Niña episodes (i.e., 34.3 months) is higher than that  
828 simulated by the two AMIP models shown in Table 2 (i.e., E1 and E2 in Table 2). As exhibited by the  
829 coupled model capable of simulating the ENSO modulation of the QBO period, Fig. 12d shows that the

Deleted: OLR anomalies

§30 contrast in the OLRA between warm and cold ENSO extremes simulated by Coupled-NINT-AP is  
831 apparently sharper than the observed one shown in Fig. 2c. In particular, the tropical convection in the  
832 central and eastern Pacific during El Niño episodes simulated by Coupled-NINT-AP is both more  
833 extensive and more intensive than that simulated by the two AMIP models shown in Figs. 12a and 12b,  
§34 which is consistent with the fact that the composite contrast in the SSTA simulated by Coupled-NINT-  
835 AP shown in Fig. 7d is substantially sharper than that prescribed in the two AMIP models shown in Fig.  
836 8a. Thus, even though the wind filtering of GWs during El Niño episodes simulated by Coupled-NINT-  
837 AP shown in Figs 12d is significantly smaller than that simulated by AMIP-OMA-SP and AMIP-

Deleted: OLR anomalies

Deleted: SST anomalies

842 OMA–AP shown in Figs 12a and 12b, respectively, the combined effect of the lower contrast in the wind  
843 filtering and the higher contrast in the amount of GW momentum fluxes generated by convective  
844 activities between warm and cold ENSO extremes over the central and eastern tropical Pacific results in  
845 a comparable ENSO modulation of the QBO period simulated by Coupled–NINT–AP to that simulated  
846 by the two AMIP models as illustrated in Table 2.

847 Finally, comparing Fig. 12c with Fig. 2c and other three panels in Fig. 12 reveals that convective  
848 activities during the warm ENSO phase simulated by the Coupled–NINT–SP model are substantially  
849 weaker than both the observed and those simulated by other three models list in Table 1. Combining the  
850 small composite OLR difference shown in Fig. 12c and the small difference in the wind filtering shown  
851 in Fig. 8c between warm and cold ENSO extremes over the central and eastern equatorial Pacific results  
852 in a low contrast in GW forcing between warm and cold ENSO phases shown in Fig. 6a, which, short of  
853 the compensating effect of the excessively amplified ENSO in Coupled–NINT–AP ensemble runs,  
854 should lead to a relatively weaker ENSO modulation of the QBO period simulated by the Coupled–  
855 NINT–SP model as illustrated in Table 2. However, this is not the whole story; and we will return to this  
856 subject in the discussion section<sup>1</sup>.

857

## 858 **6. Discussion and Conclusions**

Deleted: 5

---

<sup>1</sup> In order to test whether the difference patterns shown in section 5 are statistically robust we also use the statistics averaged over an ENSO event as our sample points to perform two-tailed tests. Figs. S3–S9 shown in the supplement demonstrate that those difference patterns are statistically significant at the 5% significance level to a large extent.

860 Both Kawatani et al. (2019) and Serva et al. (2020) pointed out that a relatively high horizontal  
861 resolution is necessary to simulate the ENSO modulation of the QBO period. Employing an Earth system  
862 model with T42 ( $\sim 2.79^\circ$ ) horizontal resolution, Kawatani et al. (2019) further demonstrated that the  
863 ENSO modulation of the QBO could not be simulated with their fixed GW sources. Serva et al. (2020)  
864 also pointed out that the reliance on stationary parameterizations of GWs is partly responsible for failing  
865 to simulate the observed modulation of the QBO by the ENSO in current climate models.

866 Rind et al. (1988) implemented various interactive GW sources in the GISS climate models. With the  
867 momentum flux of the parameterized convective waves dependent on the convective mass flux,  
868 buoyancy frequency and density at the top of the convective region, wind velocity averaged over the  
869 convective layers, etc. and with a horizontal resolution of  $2^\circ$  latitude by  $2.5^\circ$  longitude, all the four  
870 versions of GISS E2.2 models in this study can simulate the ENSO modulation of the QBO period to  
871 various degrees. For each of 19 runs conducted in this study, the absolute momentum fluxes at the source  
872 levels over the equatorial belt is larger during El Niño episodes than during La Niña episodes, leading  
873 to a shorter and longer QBO period, respectively.

874 Realistic simulation of the ENSO modulation of the QBO periods entails the realistic simulation of  
875 both the ENSO and the QBO. With the realistic SSTs specified, both the composite difference in the  
876 Walker circulation and the composite OLR difference between warm and cold ENSO extremes simulated  
877 by the two AMIP E2.2 models are close to the observed. Since the AMIP model with the “altered physics”  
878 performs better than that with the “standard physics” as far as the simulated OLR is concerned, the  
879 ensemble mean difference in the QBO period between La Niña and El Niño episodes (i.e.,  $\sim 4.5$  months)  
880 simulated by AMIP-OMA-AP is larger than that simulated by AMIP-OMA-SP (i.e.,  $\sim 3.9$  months),  
881 which indicates that convective parameterization scheme is important not only for simulating the  
882 resolved waves as pointed out by Horinouchi et al. (2003) and Lott et al. (2014), but also for

883 parameterizing GWs. However, the convective activities simulated by both AMIP E2.2 models are still  
884 inadequate over the central and eastern equatorial Pacific as compared to the observed, which may partly  
885 account for why the ensemble mean differences in the QBO period between La Niña and El Niño  
886 episodes simulated by both AMIP models are smaller than the observed difference (i.e., ~8.7 months).

887 Although the simulated Walker circulation associated with the ENSO cycle is comparable among the  
888 two coupled ocean-atmosphere models in this study, the E2.2 model with the “standard physics”  
889 performs well in its simulated SSTs which is very close to the observed while the ENSO amplitudes  
890 simulated by other model with the “altered physics” are substantially greater than the observed. Yet the  
891 model with the “standard physics” not only fails to properly simulate the shift of the strongest convection  
892 from the maritime continent during La Niña to the central and eastern equatorial Pacific during El Niño,  
893 but also grossly fail to simulate the sufficient amplitude of the OLR concomitant with the ENSO cycle.  
894 The weaker response of the Walker circulation and convective activities to the ENSO cycle together  
895 with the dislocated centers of convection concomitant to cold and warm ENSO extremes leads to the  
896 smallest ensemble mean difference in the QBO period between La Niña and El Niño episodes (i.e., ~2.7  
897 months) simulated by the Coupled–NINT–SP model. The weaker variation of the Walker circulation and  
898 the excessive change in convection compensate to give an impression of realistically simulating the  
899 ENSO modulation of the QBO period by the other model with the “altered physics”, i.e., Coupled–  
900 NINT–AP, with its ensemble mean differences in the QBO period between La Niña and El Niño episodes  
901 being ~4.8 months. However, it is worth pointing out that we don’t regard that model as the best among  
902 the four models listed in Table 1 because the relatively satisfactory results are achieved in a  
903 compensatory, thus unrealistic, way. Serva et al. (2020) conducted both the atmosphere-only and coupled  
904 historical simulations and found that the trough-to-crest amplitudes of the OLR associated with the  
905 ENSO cycle are two times larger than the observed for a few models that relatively well capture the

Deleted: s

Deleted: are

908 ENSO modulation of the QBO period, which together with our results suggests that the parameterized  
909 convection is a linchpin of realistically simulating the ENSO, the QBO, and the ENSO modulation of  
910 the QBO.

911 Intriguingly, the simulated difference in the QBO period between La Niña and El Niño is 6.2 months  
912 from the first realization simulated by Coupled–NINT–SP. However, it is not statistically significant at  
913 the 5% significance level. Meanwhile, the differences in the QBO period between La Niña and El Niño  
914 from most of the realizations simulated by Coupled–NINT–AP are apparently less than 6.2 months but  
915 are all statistically significant. To gain a deeper insight, we calculate the frequency power spectra of  
916 standardized ONIs derived from the observed and simulated SSTs. Fig. 13a depicts the power spectral  
917 densities (PSD) of standardized ONI between 1953 and 2015 derived from the NOAA ERSSTv5 SST  
918 while Fig. 13b delineates the PSD of standardized ONI between 1871 and 2013 derived from the  
919 HadISST1 dataset as used in the AMIP runs. Figs. 13a and 13b show that although the ENSO accounts  
920 for the lion’s share of SST variabilities, there is a good amount of SST variabilities on the decadal and  
921 multidecadal time scales. Fig. 13d illustrates the PSD of standardized ONI between 1871 and 2013  
922 simulated by the second realization of Coupled–NINT–AP, which demonstrates that the ENSO  
923 overwhelmingly dominates over any other noises in SST variabilities simulated by those E2.2 models  
924 with the “altered physics”. Furthermore, Fig. 13c shows the PSD of standardized ONI between 1871 and  
925 2013 simulated by the first realization of Coupled–NINT–SP. Apparently, the SST variabilities  
926 simulated by the E2.2 model with the “standard physics” are comparable to the observed, thus more  
927 realistic. The smaller ratio of the ENSO signal to the noise simulated by the first realization of Coupled–  
928 NINT–SP and the much larger ratio simulated by the second realizations of the E2.2 models with “alter  
929 physics” explain why the difference of 6.2 months in the QBO period between La Niña and El Niño

930 from the former is not statistically significant while the differences of 2.6 and 4.8 months from the latter  
931 are statistically significant as shown in Table 2.

Deleted: why

932 The rich spectrum of internal variabilities simulated by Coupled–NINT–SP, to a large degree, reflects  
933 the observed ones shown in Figs. 13a and 13b. Those large internal variabilities likely underlie why one  
934 of the historical runs simulated by Coupled–NINT–SP gives rise to a slower mean QBO phase speed  
935 during El Niño than during La Niña while other four runs from Coupled–NINT–SP do simulate a faster  
936 phase speed of the QBO during warm ENSO events. Kawatani et al. (2019) conducted two 100-yr  
937 experiments: one for a perpetual El Niño condition and the other for a perpetual La Niña condition. Their  
938 Fig. 3 shows that although the long-term mean QBO period from the El Niño run is shorter than that  
939 from the La Niña run, this is not the case for each individual year. This is because various internal  
940 variabilities exert their influence over the QBO period.

941 None of the E2.2 configurations robustly simulate an ENSO modulation of QBO amplitude,  
942 consistent with the weaker signal present in observations (Yuan et al., 2014). It is not surprising because  
943 our observational analyses show that the ENSO modulation of the QBO amplitude is not statistically  
944 significant at the 95% confidence level. In order to realistically simulate the ENSO modulation of the  
945 QBO, various aspects of climate models such as the SSTs, the Walker circulation, the parameterizations  
946 of convection and GWs need to be further improved, which is fortunately ongoing under the auspices of  
947 the SPARC Quasi-Biennial Oscillation initiative (Butchart et al., 2018).

Deleted: s

948

#### 949 **Data availability**

950 The monthly mean zonal winds from Free University of Berlin are obtained from [https://www.geo.fu-](https://www.geo.fu-berlin.de/en/met/ag/strat/produkte/qbo/index.html)  
951 [berlin.de/en/met/ag/strat/produkte/qbo/index.html](https://www.geo.fu-berlin.de/en/met/ag/strat/produkte/qbo/index.html). The NOAA ERSSTv5 SST is acquired from  
952 <https://www.ncei.noaa.gov/products/extended-reconstructed-sst>. The NCEI OLR is downloaded from

955 <https://www.ncei.noaa.gov/products/climate-data-records/outgoing-longwave-radiation-monthly>. The  
956 ERA5 monthly mean zonal winds are obtained from the ECMWF C3S at Climate Data Store:  
957 <https://cds.climate.copernicus.eu/>. The [Coupled-NINT-AP outputs](#) are available from the Earth System  
958 Grid Federation. [The data used in this paper from the other three E2.2 models are accessible at](#)  
959 <https://zenodo.org/record/8360291>.

Deleted: GISS ModelE E2.2

Deleted: data

Deleted:

Deleted: and also from the NASA Center for Climate Simulation data portal (including non-CMIP6 simulations)

### 961 **Supplementary Figures**

962 [Figs. S1–S5 are supplementary to Figs. 2–6, respectively.](#)

963 [Fig. S6 are supplementary to Fig. 8.](#)

964 [Figs. S7–S9 are supplementary to Figs. 10–12, respectively.](#)

### 966 **Author contributions**

967 All authors made equal contributions to this work.

### 969 **Competing interests**

970 The authors declare that they have no conflict of interest.

972 **Acknowledgements:** Climate modeling at GISS is supported by the NASA Modeling, Analysis and  
973 Prediction program, and resources supporting this work were provided by the NASA High-End  
974 Computing (HEC) Program through the NASA Center for Climate Simulation (NCCS) at Goddard Space  
975 Flight Center. The authors thank three anonymous reviewers for their constructive comments, which led  
976 to a significantly improved paper.

977



983 **References**

- 984 Alexander, M. J., Ortland, D. A., Grimsdell, A. W., and Kim, J.-E.: Sensitivity of Gravity Wave Fluxes  
985 to Interannual Variations in Tropical Convection and Zonal Wind, *J. Atmos. Sci.*, 74, 2701–  
986 2716, <https://doi.org/10.1175/JAS-D-17-0044.1>, 2017.
- 987 Andrews, D. G., Mahlman, J. D., and Sinclair, R. W.: Eliassen–Palm diagnostics of wave-mean flow  
988 interaction in the GFDL” SKYHI” general circulation model, *J. Atmos. Sci.*, 40, 2768–2784,  
989 [https://doi.org/10.1175/1520-0469\(1983\)040%3C2768:ETWATM%3E2.0.CO;2](https://doi.org/10.1175/1520-0469(1983)040%3C2768:ETWATM%3E2.0.CO;2), 1983.
- 990 Andrews, D. G., Holton, J. R., and Leovy, C. B.: *Middle Atmosphere Dynamics*, Academic Press, 489  
991 pp, 1987.
- 992 Angell, J. K.: On the variation in period and amplitude of the quasi-biennial oscillation in the equatorial  
993 stratosphere, 1951–85, *Mon. Weather Rev.*, 114, 2272–2278, [https://doi.org/10.1175/1520-0493\(1986\)114%3C2272:OTVIPA%3E2.0.CO;2](https://doi.org/10.1175/1520-0493(1986)114%3C2272:OTVIPA%3E2.0.CO;2), 1986.
- 995 Anstey, J. A., Banyard, T. P., Butchart, N., Coy, L., Newman, P. A., Osprey, S., and Wright, C. J.:  
996 Prospect of Increased Disruption to the QBO in a Changing Climate, *Geophys. Res. Lett.*, 48,  
997 e2021GL093058, <https://doi.org/10.1029/2021GL093058>, 2021.
- 998 Baldwin, M. P., Gray, L. J., Dunkerton, T. J., Hamilton, K., Haynes, P. H., Randel, W. J., Holton, J. R.,  
999 Alexander, M. J., Hirota, I., Horinouchi, T., Jones, D. B. A., Kinnnersley, J. S., Marquardt, C., Sato,  
1000 K., and Takahashi, M.: The Quasi-biennial oscillation, *Rev. Geophys.*, 39, 179–229,  
1001 <https://doi.org/10.1029/1999RG000073>, 2001.
- 1002 Bauer, S. E., Tsigaridis, K., Faluvegi, G., Kelley, M., Lo, K. K., Miller, R. L., Nazarenko, L., Schmidt,  
1003 G. A., and Wu, J.: Historical (1850–2014) Aerosol Evolution and Role on Climate Forcing Using  
1004 the GISS ModelE2.1 Contribution to CMIP6, *J. Adv. Model. Earth Sy.*, 12, e2019MS001978,  
1005 <https://doi.org/10.1029/2019ms001978>, 2020.

1006 Bergman, J. W. and Salby, M. L.: Equatorial wave activity derived from fluctuations in observed  
1007 convection, *J. Atmos. Sci.* 51, 3791–3806, [https://doi.org/10.1175/1520-](https://doi.org/10.1175/1520-0469(1994)051%3C3791:EWADFF%3E2.0.CO;2)  
1008 0469(1994)051%3C3791:EWADFF%3E2.0.CO;2, 1994.

1009 Bjerknes, J.: Atmospheric teleconnections from the equatorial Pacific, *Mon. Weather Rev.*, 97, 163–172,  
1010 [https://doi.org/10.1175/1520-0493\(1969\)097%3C0163:ATFTEP%3E2.3.CO;2](https://doi.org/10.1175/1520-0493(1969)097%3C0163:ATFTEP%3E2.3.CO;2), 1969.

1011 Bushell, A. C., Anstey, J. A., Butchart, N., Kawatani, Y., Osprey, S. M., Richter, J. H., Serva, F.,  
1012 Braesicke, P., Cagnazzo, C., Chen, C.-C., Chun, H.-Y., Garcia, R. R., Gray, L. J., Hamilton, K.,  
1013 Kerzenmacher, T., Kim, Y.-H., Lott, F., McLandress, C., Naoe, H., Scinocca, J., Smith, A. K.,  
1014 Stockdale, T. N., Versick, S., Watanabe, S., Yoshida, K., and Yukimoto, S.: Evaluation of the Quasi-  
1015 Biennial Oscillation in global climate models for the SPARC QBO-initiative, *Q. J. Roy. Meteor.*  
1016 *Soc.*, 1–31, <https://doi.org/10.1002/qj.3765>, 2020.

1017 Butchart, N., Anstey, J., Hamilton, K., Osprey, S., McLandress, C., Bushell, A. C., Kawatani, Y., Kim,  
1018 Y.-H., Lott, F., Scinocca, J., Stockdale, T.N., Andrews, M., Bellprat, O., Braesicke, P., Cagnazzo,  
1019 C., Chen, C.-C., Chun, H.-Y., Dobrynin, M., Garcia, R., Garcia-Serrano, J., Gray, L.J., Holt, L.,  
1020 Kerzenmacher, T., Naoe, H., Pohlmann, H., Richter, J. H., Scaife, A.A., Schenzinger, V., Serva, F.,  
1021 Versick, S., Watanabe, S., Yoshida, K. and Yukimoto, S.: Overview of experiment design and  
1022 comparison of models participating in phase 1 of the SPARC Quasi-Biennial Oscillation initiative  
1023 (QBOi), *Geoscientific Model Development*, 11, 1009–1032. [https://doi.org/10.5194/gmd-11-1009-](https://doi.org/10.5194/gmd-11-1009-2018)  
1024 2018, 2018.

1025 Calvo, N., Garcia, R. R., Randel, W. J., and Marsh, D. R.: Dynamical mechanism for the increase in  
1026 tropical upwelling in the lowermost tropical stratosphere during warm ENSO events, *J. Atmos. Sci.*,  
1027 67, 2331–2340, <https://doi.org/10.1175/2010JAS3433.1>, 2010.

1028 Cane, M. and Zebiak, S. E.: Prediction of El Niño events using a physical model, in Atmospheric and  
1029 Oceanic Variability, edited by H. Cattle, Royal Meteorological Society Press, London, 153-182,  
1030 1987.

1031 Chernick, M. R.: Bootstrap methods: A guide for practitioners and researchers, Wiley-Interscience,  
1032 369pp, 2007).

1033 Christiansen, B., Yang, S., and Madsen, M. S.: Do strong warm ENSO events control the phase of the  
1034 stratospheric QBO?, *Geophys. Res. Lett.*, 43, 10489–10495,  
1035 <https://doi.org/10.1002/2016GL070751>, 2016.

1036 Collimore, C. C., Martin, D. W., Hitchman, M. H., Huesmann, A., and Waliser, D. E.: On the  
1037 relationship between the QBO and tropical deep convection, *J. Climate*, 16, 2552–2568,  
1038 [https://doi.org/10.1175/1520-0442\(2003\)016%3C2552:OTRBTQ%3E2.0.CO;2](https://doi.org/10.1175/1520-0442(2003)016%3C2552:OTRBTQ%3E2.0.CO;2), 2003.

1039 Coy, L., Newman, P. A., Strahan, S., and Pawson, S.: Seasonal variation of the quasi-biennial oscillation  
1040 descent, *J. Geophys. Res.-Atmos.*, 125, e2020JD033077, <https://doi.org/10.1029/2020JD033077>,  
1041 2020.

1042 DallaSanta, K., Orbe, C., Rind, D., Nazarenko, L., and Jonas, J.: Dynamical and trace gas responses of  
1043 the Quasi-Biennial Oscillation to increased CO<sub>2</sub>, *J. Geophys. Res. Atmos.*, 126, e2020JD034151.  
1044 <https://doi.org/10.1029/2020JD034151>, 2021.

1045 Domeisen, D. I. V., Garfinkel, C. I., and Butler, A. H.: The Teleconnection of El Niño Southern  
1046 Oscillation to the Stratosphere, *Rev. Geophys.*, 57, 5–  
1047 47, <https://doi.org/10.1029/2018RG000596>, 2019.

1048 Garfinkel, C. I. and Hartmann, D. L.: Effects of El Niño – South- ern Oscillation and the Quasi-Biennial  
1049 Oscillation on polar tem- peratures in the stratosphere, *J. Geophys. Res.*, 112, D19112,  
1050 <https://doi.org/10.1029/2007JD008481>, 2007.

1051 Garfinkel, C. I. and Hartmann, D. L.: The influence of the quasi-biennial oscillation on the troposphere  
1052 in winter in a hierarchy of models. Part I: Simplified dry GCMs, *J. Atmos. Sci.*, 68, 1273–1289,  
1053 <https://doi.org/10.1175%2F2011JAS3665.1>, 2011a.

1054 Garfinkel, C. I. and Hartmann, D. L.: The influence of the quasi-biennial oscillation on the troposphere  
1055 in winter in a hierarchy of models. Part II: Perpetual winter WACCM runs, *J. Atmos. Sci.*, 68, 2026–  
1056 2041, <https://doi.org/10.1175%2F2011JAS3702.1>, 2011b.

1057 Geller, M. A., Zhou, T., Shindell, D., Ruedy, R., Aleinov, I., Nazarenko, L., Tausnev, N. L., Kelley, M.,  
1058 Sun, S., Cheng, Y., Field, R. D., and Faluvegi, G.: Modeling the QBO-improvements resulting from  
1059 higher-model vertical resolution, *J. Adv. Model. Earth Syst.*, 8, 1092–1105,  
1060 <https://doi.org/10.1002/2016MS000699>, 2016a.

1061 Geller, M. A., Zhou, T., and Yuan, W.: The QBO, gravity waves forced by tropical convection, and  
1062 ENSO, *J. Geophys. Res. Atmos.*, 121, 8886–8895, <https://doi.org/10.1002/2015JD024125>, 2016b.

1063 Giorgetta, M. A., Bengtson, L., and Arpe, K.: An investigation of QBO signals in the east Asian and  
1064 Indian monsoon in GCM experiments, *Climate Dynamics*, 15, 435–450,  
1065 <https://doi.org/10.1007/s003820050292>, 1999.

1066 Giorgetta, M. A., Manzini, E., and Roeckner, E., Esch, M., and Bengtsson, L.: Climatology and forcing  
1067 of the quasi-biennial oscillation in the MAECHM5 model, *J. Climate*, 19, 3882–3901,  
1068 <https://doi.org/10.1175/JCLI3830.1>, 2006.

1069 Graham, N. E. and Barnett, T. P.: Sea surface temperature, surface wind divergence, and convection over  
1070 tropical oceans, *Science*, 238, 657–659, <https://doi.org/10.1126/science.238.4827.657>, 1987.

1071 Gray, W. M.: Atlantic seasonal hurricane frequency. Part I: El Niño and 30-mb quasi-biennial oscillation  
1072 influences, *Mon. Wea. Rev.*, 112, 1649–1688, [https://doi.org/10.1175/1520-0493\(1984\)112%3C1649:ASHFPI%3E2.0.CO;2](https://doi.org/10.1175/1520-0493(1984)112%3C1649:ASHFPI%3E2.0.CO;2), 1984.

1074 Gray, W. M., Sheaffer, J. D., and Knaff, J.: Influence of the stratospheric QBO on ENSO variability, *J.*  
1075 *Meteor. Soc. Jpn.*, 70, 975–995, [https://doi.org/10.2151/jmsj1965.70.5\\_975](https://doi.org/10.2151/jmsj1965.70.5_975), 1992.

1076 Grothe, P. R., Cobb, K. M., Liguori, G., Di Lorenzo, E., Capotondi, A., Lu, Y., Cheng, H., Edwards, R.L.,  
1077 Southon, J. R., Santos, G. M., Deocampo, D. M., Lynch-Stieglitz, J., Chen, T., Sayani, H. R.,  
1078 Thompson, D. M., Conroy, J. L., Moore, A. L., Townsend, K., Hagos, M., O'Connor, G., and Toth,  
1079 L. T.: Enhanced El Niño–Southern oscillation variability in recent decades, *Geophys. Res. Lett.*, 47,  
1080 e2019GL083906, <https://doi.org/10.1029/2019GL083906>, 2019.

1081 Hamilton, K., Osprey, S., and Butchart, N.: Modeling the stratosphere’s “heartbeat,” *Eos*, 96, p. 8,  
1082 <https://doi.org/10.1029/2015EO032301>, 2015.

1083 Hamilton, K., Hertzog, A., Vial, F., and Stenchikov, G.: Longitudinal variation of the stratospheric Quasi-  
1084 Biennial Oscillation, *J. Atmos. Sci.*, 61, 383–402, [https://doi.org/10.1175/1520-](https://doi.org/10.1175/1520-0469(2004)061%3C0383:LVOTSQ%3E2.0.CO;2)  
1085 [0469\(2004\)061%3C0383:LVOTSQ%3E2.0.CO;2](https://doi.org/10.1175/1520-0469(2004)061%3C0383:LVOTSQ%3E2.0.CO;2), 2004.

1086 Hansen, F., Matthes, K., and Wahl, S.: Tropospheric QBO–ENSO interactions and differences between  
1087 the Atlantic and Pacific, *J. Climate*, 29, 1353–1368, <https://doi.org/10.1175/JCLI-D-15-0164.1>,  
1088 2016

1089 Hasebe, F.: Quasi-biennial oscillations of ozone and diabatic circulation in the equatorial stratosphere, *J.*  
1090 *Atmos. Sci.*, 51, 729–745, [https://doi.org/10.1175/1520-](https://doi.org/10.1175/1520-0469(1994)051%3c0729:QBOOOA%3e2.0.CO;2)  
1091 [0469\(1994\)051%3c0729:QBOOOA%3e2.0.CO;2](https://doi.org/10.1175/1520-0469(1994)051%3c0729:QBOOOA%3e2.0.CO;2), 1994.

1092 Haynes, P. H., McIntyre, M. E., Shepherd, T. G., Marks, C. J., and Shine, K. P.: On the “Downward  
1093 Control” of Extratropical Diabatic Circulations by Eddy-Induced Mean Zonal Forces, *J. Atmos. Sci.*,  
1094 48, 651–678, [https://doi.org/10.1175/1520-0469\(1991\)048%3C0651:OTCOED%3E2.0.CO;2](https://doi.org/10.1175/1520-0469(1991)048%3C0651:OTCOED%3E2.0.CO;2), 1991.

1095 Hersbach, H., Bell, B., Berrisford, P., Hirahara, S., Horányi, A., Muñoz-Sabater, J., Nicolas, J., Peubey,  
1096 C., Radu, R., Schepers, D., Simmons, A., Soci, C., Abdalla, S., Abellan, X., Balsamo, G., Bechtold,

1097 P., Biavati, G., Bidlot, J., Bonavita, M., Chiara, G., Dahlgren, P., Dee, D., Diamantakis, M., Dragani,  
1098 R., Flemming, J., Forbes, R., Fuentes, M., Geer, A., Haimberger, L., Healy, S., Hogan, R. J., Hólm,  
1099 E., Janisková, M., Keeley, S., Laloyaux, P., Lopez, P., Lupu, C., Radnoti, G., Rosnay, P., Rozum, I.,  
1100 Vamborg, F., Villaume, S., and Thépaut, J.-N.: The ERA5 global reanalysis, *Q. J. Roy. Meteor. Soc.*,  
1101 online first, <https://doi.org/10.1002/qj.3803>, 2020.

1102 Hitchman, M. H., and Huesmann, A. S.: Seasonal influence of the quasi-biennial oscillation on  
1103 stratospheric jets and Rossby wave breaking, *J. Atmos. Sci.*, 66, 935–946,  
1104 <https://doi.org/10.1175%2F2008JAS2631.1>, 2009.

1105 Ho, C.-H., Kim, H.-S., Jeong, J.-H., and Son, S.-W.: Influence of stratospheric quasi-biennial oscillation  
1106 on tropical cyclone tracks in the western North Pacific, *Geophys. Res. Lett.*, 36, L06702,  
1107 <http://dx.doi.org/10.1029/2009GL037163>, 2009.

1108 Holton, J.: Waves in the equatorial stratospheric generated by tropospheric heat resources, *J. Atmos. Sci.*,  
1109 27, 368–375, [https://doi.org/10.1175/1520-0469\(1972\)029%3C0368:WITESG%3E2.0.CO;2](https://doi.org/10.1175/1520-0469(1972)029%3C0368:WITESG%3E2.0.CO;2), 1972.

1110 Holton, J. R. and Lindzen, R. S.: An updated theory for the quasi-biennial cycle of the tropical  
1111 stratosphere, *J. Atmos. Sci.*, 29, 1076–1080, [https://doi.org/10.1175/1520-0469\(1972\)029%3c1076:AUTFTQ%3e2.0.CO;2](https://doi.org/10.1175/1520-0469(1972)029%3c1076:AUTFTQ%3e2.0.CO;2), 1972.

1113 Holton, J. R. and Tan, H.: The Influence of the equatorial quasi-biennial oscillation on the global  
1114 circulation at 50 mb, *J. Atmos. Sci.*, 37, 2200–2208, [https://doi.org/10.1175/1520-0469\(1980\)037%3c2200:TIOTEQ%3e2.0.CO;2](https://doi.org/10.1175/1520-0469(1980)037%3c2200:TIOTEQ%3e2.0.CO;2), 1980.

1116 Horinouchi, T., Pawson, S., Shibata, K., Manzini, E., Giorgetta, M., and Sassi, F.: Tropical cumulus  
1117 convection and upward propagating waves in middle-atmospheric GCMs, *J. Atmos. Sci.*, 60, 2765–  
1118 2782, [https://doi.org/10.1175/1520-0469\(2003\)060%3C2765:TCCA UW%3E2.0.CO;2](https://doi.org/10.1175/1520-0469(2003)060%3C2765:TCCA UW%3E2.0.CO;2), 2003.

1119 Hu, Z.-Z., Huang, B., Kinter, J. L., Wu, Z., and Kumar, A.: Connection of the stratospheric QBO with  
1120 global atmospheric general circulation and tropical SST. Part II: Interdecadal variations, *Climate*  
1121 *Dynamics*, 38, 25–43, <https://doi.org/10.1007/s00382-011-1073-6>, 2012.

1122 Huang, B. H., Hu, Z. Z., Kinter, J. L., Wu, Z. H., and Kumar, A.: Connection of stratospheric QBO with  
1123 global atmospheric general circulation and tropical SST. Part I: Methodology and composite life  
1124 cycle, *Climate Dynamics*, 38, 1–23, <https://doi.org/10.1007/s00382-011-1250-7>, 2012.

1125 Huang, B., Thorne, P. W., Banzon, V. F., Boyer, T., Chepurin, G., Lawrimore, J. H., Menne M. J., Smith,  
1126 T. M., Vose R. S., and Zhang, H. M.: Extended reconstructed sea surface temperature, version 5  
1127 (ERSSTv5): upgrades, validations, and intercomparisons, *J. Climate*, 30, 8179–  
1128 8205, <https://doi.org/10.1175/JCLI-D-16-0836.1>, 2017.

1129 Kang, M.-J., Chun, H.-Y., Kim, Y.-H., Preusse, P., and Ern, M.: Momentum flux of convective gravity  
1130 waves derived from an offline gravity wave parameterization. Part II: Impacts on the Quasi-Biennial  
1131 Oscillation, *J. Atmos. Sci.*, 75, 3753–3775, <https://doi.org/10.1175/JAS-D-18-0094.1>, 2018.

1132 Kawatani, Y, Lee, J. N., and Hamilton, K.: Interannual variations of stratospheric water vapor in MLS  
1133 observations and climate model simulations, *J. Atmos. Sci.*, 71, 4072–4085,  
1134 <https://doi.org/10.1175/JAS-D-14-0164.1>, 2014.

1135 Kawatani, Y., Hamilton, K., Sato, K., Dunkerton, T. J., Watanabe, S., and Kikuchi, K.: ENSO Modulation  
1136 of the QBO: Results from MIROC Models with and without Nonorographic Gravity Wave  
1137 Parameterization, *J. Atmos. Sci.*, 76, 3893–3917, <https://doi.org/10.1175/JAS-D-19-0163.1>, 2019.

1138 Kelley, M., Schmidt, G. A., Nazarenko, L. S., Bauer, S. E., Ruedy, R., Russell, G. L., Ackerman, A. S.,  
1139 Aleinov, I., Bauer, M., Bleck, R., Canuto, V., Cesana, G., Cheng, Y., Clune, T. L., Cook, B. I., Cruz,  
1140 C. A., Del Genio, A. D., Elsaesser, G. S., Faluvegi, G., Kiang, N. Y., Kim, D., Lacis, A. A.,  
1141 Leboissetier, A., LeGrande, A. N., Lo, K. K., Marshall, J., Matthews, E. E., McDermid, S., Mezuman,

1142 K., Miller, R. L., Murray, L. T., Oinas, V., Orbe, C., Pérez, C., García-Pando, C., Perlwitz, J. P.,  
1143 Puma, M. J., Rind, D., Romanou, A., Shindell, D. T., Sun, S., Tausnev, N., Tsigaridis, K., Tselioudis,  
1144 G., Weng, E., Wu, J., and Yao, M.-S.: GISS-E2.1: Configurations and climatology, *J. Adv. Model.*  
1145 *Earth Sy.*, 12, e2019MS002025, <https://doi.org/10.1029/2019MS002025>, 2020.

1146 Kumar V., Yoden, S., and Hitchman, M. H.: QBO and ENSO effects on the mean meridional circulation,  
1147 polar vortex, subtropical westerly jets, and wave patterns during boreal winter, *J. Geophys. Res.* 127,  
1148 e2022JD036691, <https://doi.org/10.1029/2022JD036691>, 2022.

1149 Labitzke, K.: On the interannual variability of the middle stratosphere during the northern winters, *J.*  
1150 *Meteorol. Soc. Jpn.*, 80, 963–971, [http://doi.org/10.2151/jmsj1965.60.1\\_124](http://doi.org/10.2151/jmsj1965.60.1_124), 1982.

1151 Liess, S. and Geller, M. A.: On the relationship between QBO and distribution of tropical deep  
1152 convection, *J. Geophys. Res.*, 117, D03108, <http://dx.doi.org/10.1029/2011JD016317>, 2012.

1153 Lindzen, R. S. and Holton, J. R.: A theory of the quasi-biennial oscillation, *J. Atmos. Sci.*, 25, 1095–  
1154 1107, [https://doi.org/10.1175/1520-0469\(1968\)025%3C1095:ATOTQB%3E2.0.CO;2](https://doi.org/10.1175/1520-0469(1968)025%3C1095:ATOTQB%3E2.0.CO;2), 1968.

1155 Lott, F., Denvil, S., Butchart, N., Cagnazzo, C., Giorgetta, M. A., Hardiman, S. C., Manzini, E.,  
1156 Krismer, T., Duvel, J.-P., Maury, P., Scinocca, J. F., Watanabe, S., and Yukimoto, S.: Kelvin  
1157 and Rossby-gravity wave packets in the lower stratosphere of some high-top CMIP5 models, *J.*  
1158 *Geophys. Res.*, 119, 2156–2173, <https://doi.org/10.1002/2013JD020797>, 2014.

1159 Maruyama, T. and Tsuneoka, Y.: Anomalously short duration of the QBO at 50 hPa of the easterly wind  
1160 phase in 1987 and its relationship to an El Niño event, *J. Meteorol. Soc. Jpn.*, 66, 629–634,  
1161 [https://doi.org/10.2151/jmsj1965.66.4\\_629](https://doi.org/10.2151/jmsj1965.66.4_629), 1988.

1162 Miller, R. L., Schmidt, G. A., Nazarenko, L. S., Bauer, S. E., Kelley, M., Ruedy, R., Russell, G. L.,  
1163 Ackerman, A. S., Aleinov, I., Bauer, M., Bleck, R., Canuto, V., Cesana, G., Cheng, Y., Clune, T. L.,  
1164 Cook, B. I., Cruz, C. A., Del Genio, A. D., Elsaesser, G. S., Faluvegi, G., Kiang, N. Y., Kim, D.,



1165 Lacis, A. A., Leboissetier, A., LeGrande, A. N., Lo, K. K., Marshall, J., Matthews, E. E., McDermid,  
1166 S., Mezuman, K., Murray, L. T., Oinas, V., Orbe, C., Pérez García-Pando, C., Perlwitz, J. P., Puma,  
1167 M. J., Rind, D., Romanou, A., Shindell, D. T., Sun, S., Tausnev, N., Tsigaridis, K., Tselioudis, G.,  
1168 Weng, E., Wu, J., and Yao, M. S.: CMIP6 Historical Simulations (1850–2014) With GISS-E2.1, J.  
1169 Adv. Model. Earth Syst., 13, e2019MS002034, <https://doi.org/10.1029/2019MS002034>, 2021.

1170 Moser, B. K. and Stevens, G. R.: Homogeneity of variance in the two-sample means test, Am. Stat., 46,  
1171 19–21, <https://doi.org/10.1080/00031305.1992.10475839>, 1992.

1172 Naujokat, B.: An update of the observed quasi-biennial oscillation of the stratospheric winds over the  
1173 tropics, J. Atmos. Sci., 43, 1873–1877, [https://doi.org/10.1175/1520-](https://doi.org/10.1175/1520-0469(1986)043%3C1873:AUOTOQ%3E2.0.CO;2)  
1174 [0469\(1986\)043%3C1873:AUOTOQ%3E2.0.CO;2](https://doi.org/10.1175/1520-0469(1986)043%3C1873:AUOTOQ%3E2.0.CO;2), 1986.

1175 Nazarenko, L. S., Tausnev, N., Russell, G. L., Rind, D., Miller, R. L., Schmidt, G. A., Bauer, S. E., Kelley,  
1176 M., Ruedy, R., Ackerman, A. S., Aleinov, I., Bauer, M., Bleck, R., Canuto, V., Cesana, G., Cheng,  
1177 Y., Clune, T. L., Cook, B. I., Cruz, C. A., Del Genio, A. D., Elsaesser, G. S., Faluvegi, G., Kiang, N.  
1178 Y., Kim, D., Lacis, A. A., Leboissetier, A., LeGrande, A. N., Lo, K. K., Marshall, J., Matthews, E.  
1179 E., McDermid, S., Mezuman, K., Murray, L. T., Oinas, V., Orbe, C., Pérez García-Pando, C.,  
1180 Perlwitz, J. P., Puma, M. J., Romanou, A., Shindell, D. T., Sun, S., Tsigaridis, K., Tselioudis, G.,  
1181 Weng, E., Wu, J., and Yao, M.-S.: Future Climate Change Under SSP Emission Scenarios With  
1182 GISS-E2.1, J. Adv. Model. Earth Syst., 14,  
1183 e2021MS002871, <https://doi.org/10.1029/2021MS002871>, 2022.

1184 Oort, A. H. and Yienger, J. J.: Observed interannual variability in the Hadley circulation and its  
1185 connection to ENSO, J. Climate, 9, 2751–2767, [https://doi.org/10.1175/1520-](https://doi.org/10.1175/1520-0442(1996)009<2751:Oivith>2.0.Co;2)  
1186 [0442\(1996\)009<2751:Oivith>2.0.Co;2](https://doi.org/10.1175/1520-0442(1996)009<2751:Oivith>2.0.Co;2), 1996.

1187 Orbe, C., Rind, D., Jonas, J., Nazarenko, L., Faluvegi, G., Murray, L.T., Shindell, D.T., Tsigaridis, K.,  
1188 Zhou, T., Kelley, M., and Schmidt, G.: GISS Model E2.2: A climate model optimized for the middle  
1189 atmosphere. Part 2: Validation of large-scale transport and evaluation of climate response, *J.*  
1190 *Geophys. Res. Atmos.*, 125, e2020JD033151, <https://doi.org/10.1029/2020JD033151>, 2020.

1191 Philander, S. G. H.: El Niño, La Niña, and the Southern Oscillation, Academic Press, San Diego, 293pp.,  
1192 1990.

1193 Plumb, R. A.: The interaction of two internal waves with the mean flow: Implications for the theory of  
1194 the quasi-biennial oscillation, *J. Atmos. Sci.*, 34, 1847–1858, <https://doi.org/10.1175/1520->  
1195 [0469\(1977\)034<1847:TIOIWI>2.0.CO;2](https://doi.org/10.1175/1520-0469(1977)034<1847:TIOIWI>2.0.CO;2), 1977.

1196 Rao, J., Garfinkel, C. I., and White, I. P.: Impact of the Quasi-Biennial Oscillation on the Northern Winter  
1197 Stratospheric Polar Vortex in CMIP5/6 Models, *J. Climate*, 33, 4787–  
1198 4813, <https://doi.org/10.1175/JCLI-D-19-0663.1>, 2020a.

1199 Rao, J., Garfinkel, C. I., and White, I. P.: Projected strengthening of the extratropical surface impacts of  
1200 the stratospheric quasi-biennial oscillation, *Geophys. Res. Lett.*, 47,  
1201 e2020GL089149, <https://doi.org/10.1029/2020GL089149>, 2020b.

1202 Rao, J., Garfinkel, C. I., and White, I. P.: Development of the Extratropical Response to the Stratospheric  
1203 Quasi-Biennial Oscillation, *J. Climate*, 34, 7239–7255, <https://doi.org/10.1175/JCLI-D-20-0960.1>  
1204 2021.

1205 Rao, J., Garfinkel, C. I., White, I. P., and Schwartz, C.: How does the Quasi-Biennial Oscillation affect the  
1206 boreal winter tropospheric circulation in CMIP5/6 models?, *J. Climate*, 33, 8975–8996,  
1207 <https://doi.org/10.1175/JCLI-D-20-0024.1>, 2020c.

1208 Rayner, N. A., Parker, D. E., Horton, E. B., Folland, C. K., Alexander, L. V., Rowell, D. P., Kent, E. C.,  
1209 and Kaplan, A.: Global analyses of sea surface temperature, sea ice, and night marine air temperature

1210 since the late nineteenth century, *J. Geophys. Res.*, 108, 4407,  
1211 <https://doi.org/10.1029/2002JD002670>, 2003.

1212 Richter, J. H., Solomon, A., and Bacmeister, J. T.: On the simulation of the quasi-biennial oscillation in  
1213 the Community Atmosphere Model, version 5, *J. Geophys. Res.-Atmos.*, 119, 3045–  
1214 3062, <https://doi.org/10.1002/2013JD021122>, 2014.

1215 Richter, J. H., Anstey, J. A., Butchart, N., Kawatani, Y., Meehl, G. A., Osprey, S., and Simpson, I. R.:  
1216 Progress in simulating the quasi-biennial oscillation in CMIP models, *J. Geophys. Res.-Atmos.*, 125,  
1217 e2019JD032362, <https://doi.org/10.1029/2019JD032362>, 2020.

1218 Rind, D., Lerner, J., Jonas, J., and McLinden, C.: Effects of resolution and model physics on tracer  
1219 transports in the NASA Goddard Institute for Space Studies general circulation models, *J. Geophys.*  
1220 *Res.*, 112, D09315, <https://doi.org/10.1029/2006JD007476>, 2007.

1221 Rind, D., Suozzo, R., Balachandran, N. K., Lacis, A., and Russell, G.: The GISS global climate-middle  
1222 atmosphere model. Part I: Model structure and climatology, *J. Atmos. Sci.*, 45, 329–370,  
1223 [https://doi.org/10.1175/1520-0469\(1988\)045%3C0329:TGGCMA%3E2.0.CO;2](https://doi.org/10.1175/1520-0469(1988)045%3C0329:TGGCMA%3E2.0.CO;2), 1988.

1224 Rind, D., Jonas, J., Balachandran, N., Schmidt, G., and Lean, J.: The QBO in two GISS global climate  
1225 models: 1. Generation of the QBO, *J. Geophys. Res. Atmos.*, 119, 8798–8824,  
1226 <https://doi.org/10.1002/2014JD021678>, 2014.

1227 Rind, D., Orbe, C., Jonas, J., Nazarenko, L., Zhou, T., Kelley, M., Lacis, A., Shindell, D., Faluvegi,  
1228 Russell, G., Bauer, M., Schmidt, G., Romanou, A., and Tausnev, N.: GISS Model E2.2: A climate  
1229 model optimized for the middle atmosphere — Model structure, climatology, variability and climate  
1230 sensitivity, *J. Geophys. Res. Atmos.*, 125, e2019JD032204, <https://doi.org/10.1029/2019JD032204>,  
1231 2020.

1232 Salby, M. L.: *Physics of the Atmosphere and Climate*, Cambridge University Press, New York,  
1233 <https://doi.org/10.1017/CBO9781139005265>, 2012.

1234 Salby, M. L. and Garcia, R. R.: Transient response to localized episodic heating in the tropics, Part 1:  
1235 excitation and short-time near-field behavior, *J. Atmos. Sci.*, 44, 458–498,  
1236 [https://doi.org/10.1175/1520-0469\(1987\)044%3C0458:TRTLEH%3E2.0.CO;2](https://doi.org/10.1175/1520-0469(1987)044%3C0458:TRTLEH%3E2.0.CO;2), 1987.

1237 Sarachik, E. S. and Cane, M. A.: *The El Niño-Southern Oscillation Phenomenon*, Cambridge University  
1238 Press, Cambridge, 364pp., 2010.

1239 Scaife, A. A., Butchart, N., Warner, C. D., Stainforth, D., Norton, W., and Austin, J.: Realistic quasi-  
1240 biennial oscillations in a simulation of the global climate, *Geophys. Res. Lett.*, 27, 3481–3484,  
1241 <https://doi.org/10.1029/2000GL011625>, 2000.

1242 Schirber, S., Manzini, E., Krismer, T. and Giorgetta, M.: The Quasi-Biennial Oscillation in a warmer  
1243 climate: sensitivity to different gravity wave parameterizations, *Climate Dynamics*, 45, 825–  
1244 836, <https://doi.org/10.1007/s00382-014-2314-2>, 2015.

1245 Schmidt, G. A., Kelley, M., Nazarenko, L., Ruedy, R., Russell, G. L., Aleinov, I., Bauer, M., Bauer, S.  
1246 E., Bhat, M. K., Bleck, R., Canuto, V., Chen, Y.-H., Cheng, Y., Clune, T. L., Del Genio, A., de  
1247 Fainchtein, R., Faluvegi, G., Hansen, J. E., Healy, R. J., Kiang, N. Y., Koch, D., Lacis, A. A.,  
1248 LeGrande, A. N., Lerner, J., Lo, K. K., Matthews, E. E., Menon, S., Miller, R. L., Oinas, V.,  
1249 Oloso, A. O., Perlwitz, J. P., Puma, M. J., Putman, W. M., Rind, D., Romanou, A., Sato, M.,  
1250 Shindell, D. T., Sun, S., Syed, R. A., Tausnev, N., Tsigaridis, K., Unger, N., Voulgarakis, A.,  
1251 Yao, M.-S., and Zhang, J.: Configuration and assessment of the GISS ModelE2 contributions to  
1252 the CMIP5 archive, *J. Adv. Model. Earth Syst.*, 6, 141–  
1253 184, <https://doi.org/10.1002/2013MS000265>, 2014.

1254 Scott, R. K. and Haynes, P. H.: Internal interannual variability of the extratropical stratospheric  
1255 circulation: The low-latitude flywheel, *Q. J. Roy. Meteor. Soc.*, 124, 2149–  
1256 2173, <https://doi.org/10.1002/qj.49712455016>, 1998.

1257 Serva, F., Cagnazzo, C., Christiansen, B., and Yang, S.: The influence of ENSO events on the  
1258 stratospheric QBO in a multi-model ensemble, *Climate Dynamics*, 54, 2561–2575,  
1259 <https://doi.org/10.1007/s00382-020-05131-7>, 2020.

1260 Simpson, I. R., Shepherd, T. G., and Sigmond, M.: Dynamics of the lower stratospheric circulation  
1261 response to ENSO, *J. Atmos. Sci.*, 68, 2537–2556, <https://doi.org/10.1175/JAS-D-11-05.1>, 2011.

1262 Sullivan, S. C., Schiro, K. A., Stubenrauch, C., and Gentine, P.: The response of tropical organized  
1263 convection to El Niño warming, *J. Geophys. Res.-Atmos.*, 124, 8481–  
1264 8500, <https://doi.org/10.1029/2019JD031026>, 2019.

1265 Taguchi, M.: Observed connection of the stratospheric quasi-biennial oscillation with El Niño–Southern  
1266 Oscillation in radiosonde data, *J. Geophys. Res.*, 115,  
1267 D18120, <https://doi.org/10.1029/2010JD014325>, 2010.

1268 Trepte, C. R. and Hitchman, M. H.: Tropical stratospheric circulation deduced from satellite aerosol data,  
1269 *Nature*, 355, 626–628, <https://doi.org/10.1038/355626a0>, 1992.

1270 Tsuda, T., Ratnam, M. V., Alexander, S. P., Kozu, T., and Takayabu, Y.: Temporal and spatial  
1271 distributions of atmospheric wave energy in the equatorial stratosphere revealed by GPS radio  
1272 occultation temperature data obtained with the CHAMP Satellite during 2001–2006, *Earth Planets  
1273 Space*, 61, 525–533, <https://doi.org/10.1186/BF03353169>, 2009.

1274 Wallace, J., Panetta, R., and Estberg, J.: Representation of the equatorial stratospheric quasi- biennial  
1275 oscillation in EOF phase space, *J. Atmos. Sci.*, 50, 1751–1762, [https://doi.org/10.1175/1520-0469\(1993\)050<1751:ROTESQ>2.0.CO;2](https://doi.org/10.1175/1520-0469(1993)050<1751:ROTESQ>2.0.CO;2), 1993.

1277 Watanabe, S., Kawatani, Y., Tomikawa, Y., Miyazaki, K., Takahashi, M., and Sato, K.: General aspects  
1278 of a T213L256 middle atmosphere general circulation model, *J. Geophys. Res.-Atmos.*, 113,  
1279 D12110, <https://doi.org/10.1029/2008JD010026>, d12110, 2008.

1280 Wang, C., Deser, C., Yu, J.-Y., DiNezio, P., and Clement, A.: El Niño–Southern Oscillation (ENSO): A  
1281 review. In *Reefs of the Eastern Pacific*, Springer Sci. Publish., 85–106, [https://doi.org/10.1007/978-](https://doi.org/10.1007/978-94-017-7499-4_4)  
1282 94-017-7499-4\_4, 2016.

1283 Xu, J.-S., On the relationship between the stratospheric quasi-biennial oscillation and the tropospheric  
1284 southern oscillation, *J. Atmos. Sci.*, 49, 725–734, [https://doi.org/10.1175/1520-](https://doi.org/10.1175/1520-0469(1992)049<0725:OTRBTS>2.0.CO;2)  
1285 0469(1992)049<0725:OTRBTS>2.0.CO;2, 1992.

1286 Yoden, S., Kumar, V., Dhaka, S., and Hitchman, M.: Global monsoon systems and their modulation by  
1287 the equatorial Quasi-Biennial Oscillation, *MAUSAM*, 74, 239–252,  
1288 <https://doi.org/10.54302/mausam.v74i2.5948>, 2023.

1289 Yoo, C. and Son, S.-W.: Modulation of the boreal wintertime Madden-Julian oscillation by the  
1290 stratospheric quasi-biennial oscillation, *Geophys. Res. Lett.*, 43, 1392–1398,  
1291 <https://doi.org/10.1002%2F2016GL067762>, 2016.

1292 Yu, J.-Y. and Mechoso, C. R.: A coupled atmosphere–ocean GCM study of the ENSO, *J. Climate*,  
1293 14, 2329–2350, [https://doi.org/10.1175/1520-0442\(2001\)014%3C2329:ACAOGS%3E2.0.CO;2](https://doi.org/10.1175/1520-0442(2001)014%3C2329:ACAOGS%3E2.0.CO;2),  
1294 2001.

1295 Yuan, W., Geller, M. A., and Love, P. T.: ENSO influence on QBO modulations of the tropical  
1296 tropopause, *Q. J. Roy. Meteorol. Soc.*, 140, 1670–1676, <https://doi.org/10.1002/qj.2247>, 2014.

1297 Zawodny, J. M. and McCormick, M. P.: Stratospheric Aerosol and Gas Experiment II measurements of  
1298 the quasi-biennial oscillations in ozone and nitrogen dioxide, *J. Geophys. Res.*, 96, 9371– 9377,  
1299 <http://dx.doi.org/10.1029/91JD00517>, 1991.

1300 Zhao, Y. and Sun, D.-Z.: ENSO asymmetry in CMIP6 models, *J. Climate*, 5555–5572,  
1301 <https://doi.org/10.1175/JCLI-D-21-0835.1>, 2022.

1302 Zhang, C.: Large-scale variability of atmospheric deep convection in relation to sea surface temperature  
1303 in the tropics, *J. Climate*, 6, 1898–1913, [https://doi.org/10.1175/1520-](https://doi.org/10.1175/1520-0442(1993)006<1898:LSVOAD>2.0.CO;2)  
1304 [0442\(1993\)006<1898:LSVOAD>2.0.CO;2](https://doi.org/10.1175/1520-0442(1993)006<1898:LSVOAD>2.0.CO;2), 1993.

1305

**Table 1** The model configurations and respective ensemble simulations

Model configuration	Simulation	CMIP6 archive tag	Period	Ensemble size	Ensemble name
AMIP-OMA-SP	Historical AMIP	N/A	1850–2014	5	E1
AMIP-OMA-AP	Historical AMIP	N/A*	1850–2014	4	E2
Coupled-NINT-SP	CMIP6 Historical	N/A	1850–2014	5	E3
Coupled-NINT-AP	CMIP6 Historical	E2-2-G.historical.r[1-5]i1p1f1	1850–2014	5	E4

\*E2-2-G.amip.r[1-5]i1p3f1 in the CMIP6 archive are the outputs of the same model but range from 1979 to 2014.

Deleted: #

Deleted: # Coupled-NINT-SP outputs follow the CMIP6 protocol and naming. Four of five runs are available from NCCS portal at

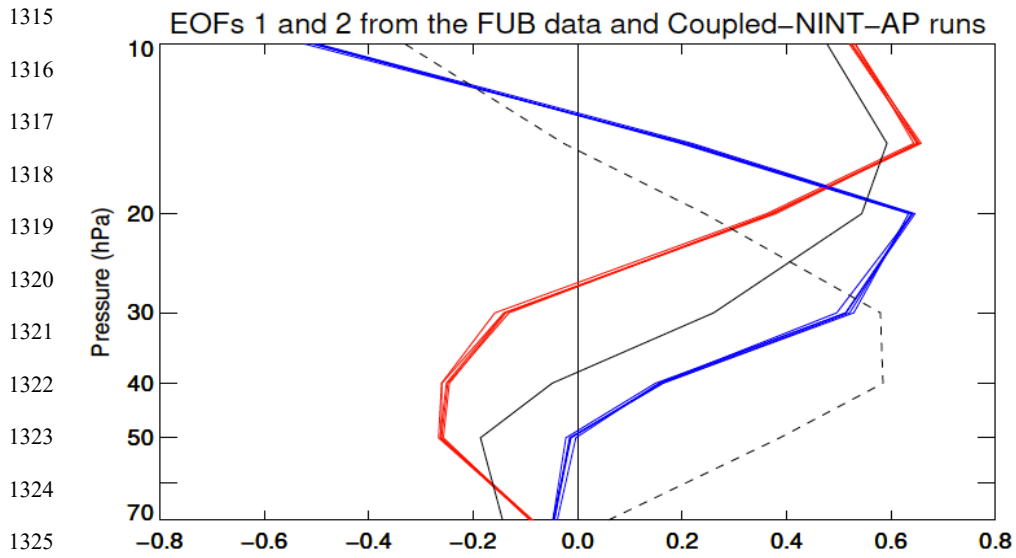
[https://portal.nccs.nasa.gov/datashare/giss\\_cmip6/CMIP/NASA-GISS/GISS-E2.2.1-G/](https://portal.nccs.nasa.gov/datashare/giss_cmip6/CMIP/NASA-GISS/GISS-E2.2.1-G/) ... [1]



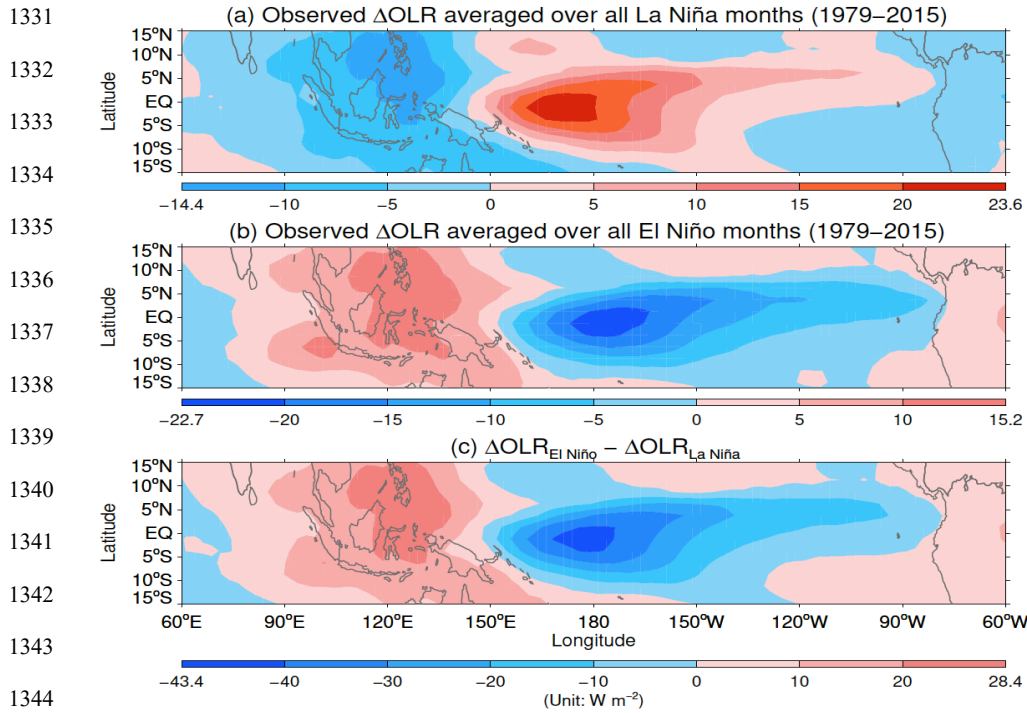
**Table 2** The ENSO influence on the QBO period

Member		r1			r2			r3			r4			r5		
ENSO Phase		EL	LA	EL-LA	EL	LA	EL-LA	EL	LA	EL-LA	EL	LA	EL-LA	EL	LA	EL-LA
Period (month)	E1	31.1	34.0	<b>(-2.9)</b>	34.9	35.9	-1.0	29.4	32.9	-3.5	29.7	36.7	<b>(-7.0)</b>	30.5	35.7	<b>(-5.2)</b>
	E2	33.1	36.5	<b>(-3.4)</b>	31.5	35.6	<b>(-4.1)</b>	32.1	35.4	-3.2	29.4	36.8	<b>(-7.4)</b>	n/a	n/a	n/a
	E3	27.5	33.7	-6.2	28.0	30.5	-2.5	30.5	29.8	0.7	30.0	31.5	-1.5	28.2	32.0	-3.8
	E4	31.2	35.0	<b>(-3.8)</b>	29.8	32.4	<b>(-2.6)</b>	29.7	35.4	<b>(-5.7)</b>	28.0	34.7	<b>(-6.7)</b>	28.0	33.4	<b>(-5.4)</b>

E[1-4] denote the ensemble simulations AMIP-OMA-SP, AMIP-OMA-AP, Coupled-NINT-SP, and Coupled-NINT-AP, respectively. r[1-5] indicate the ensemble members of those simulations. EL and LA are short for El Niño than during La Niña, respectively. The numbers in parentheses denote being statistically significantly different from zero at the 5% significance level.



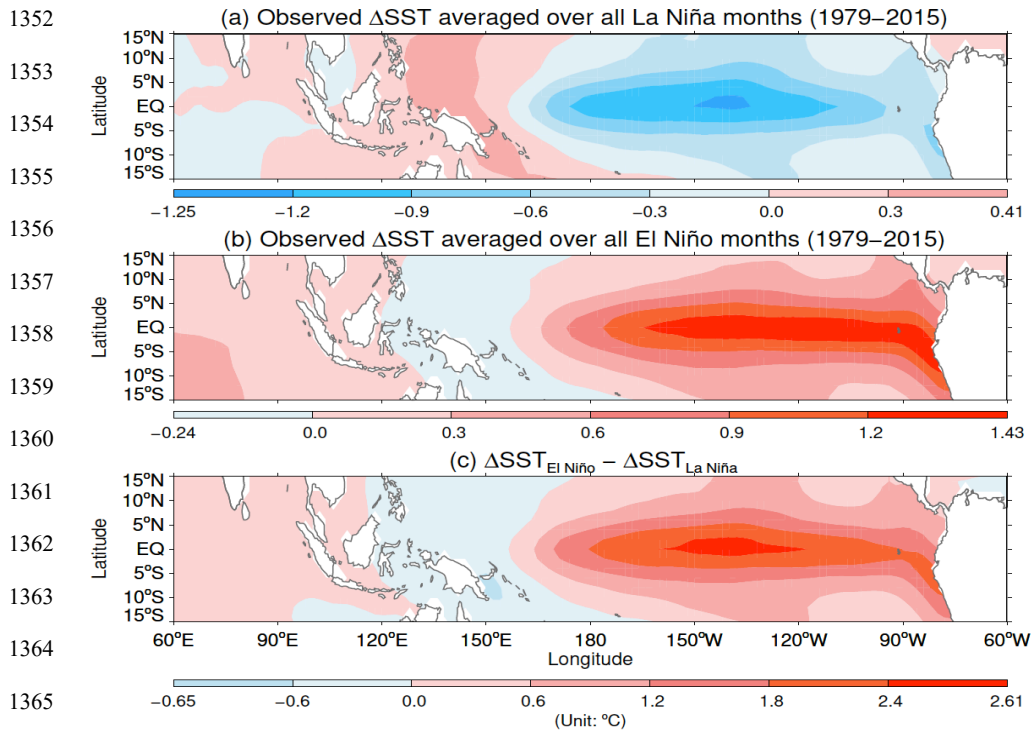
1326 **Fig. 1.** Black lines depict the first (solid) and second (dashed) orthonormal eigenvectors derived from  
 1327 the monthly FUB zonal wind anomalies between 1953 and 2015. Colored lines delineate the first (red)  
 1328 and second (blue) orthonormal eigenvectors derived from the deseasonalized and smoothed equatorial  
 1329 zonal mean zonal winds between 1873 and 2013 from the five Coupled-NINT-AP runs.  
 1330



1345 **Fig. 2.** Mean OLR deviations from climatology for (a) La Niña and (b) El Niño conditions over the  
 1346 tropical Indian and Pacific oceans. (c) Differences of mean OLRA between El Niño and La Niña  
 1347 conditions. The mean composite OLRA and their differences are derived from the datasets provided by  
 1348 NOAA NCEI.  
 1349

Deleted: OLR anomalies

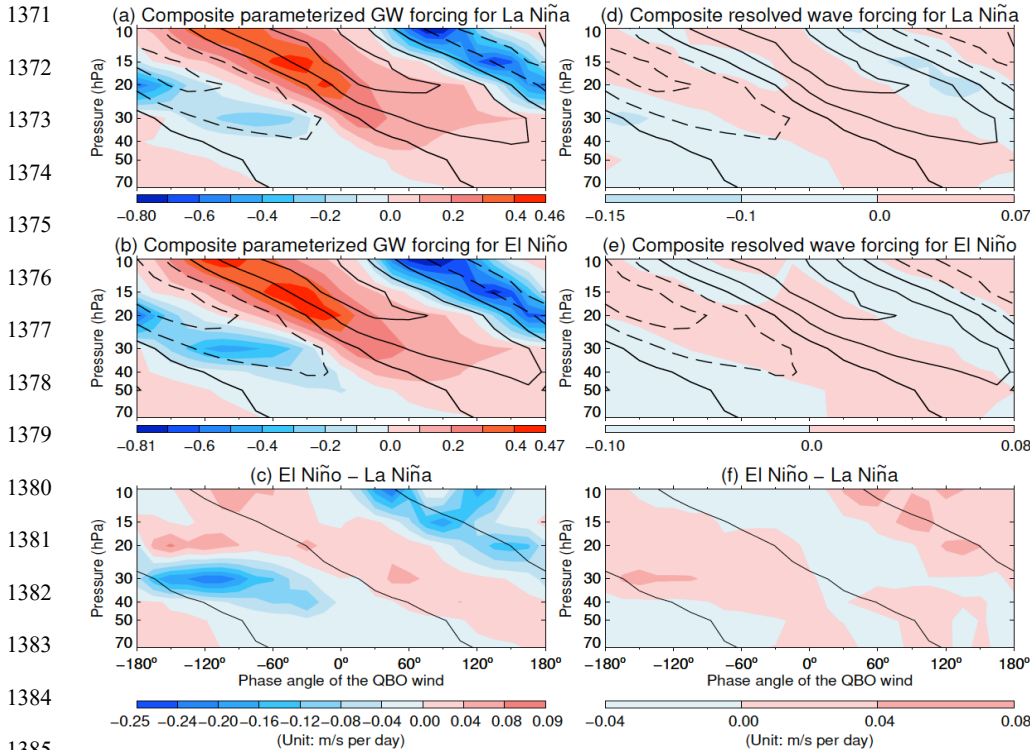
Deleted: OLR anomalies



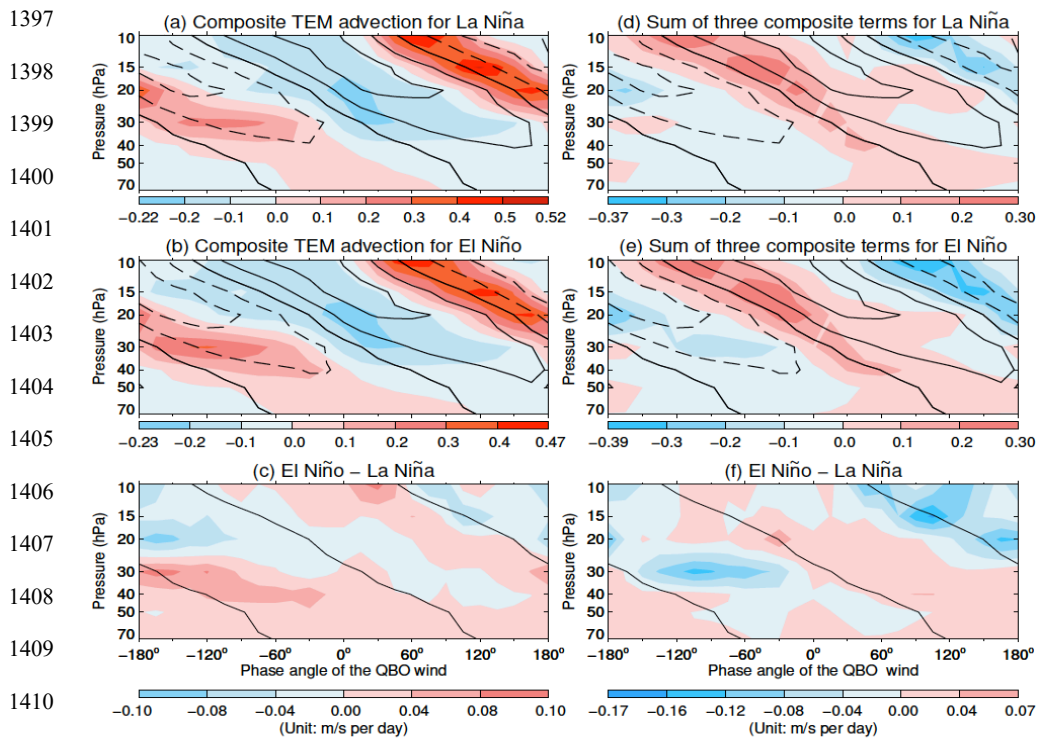
1366 **Fig. 3.** Mean SST deviations from climatology for (a) La Niña and (b) El Niño conditions over the tropical  
 1367 Indian and Pacific oceans. (c) Differences of mean SSTA between El Niño and La Niña conditions. The  
 1368 mean composite SSTA and their differences are derived from the NOAA ERSSTv5 SST.

Deleted: SST anomalies

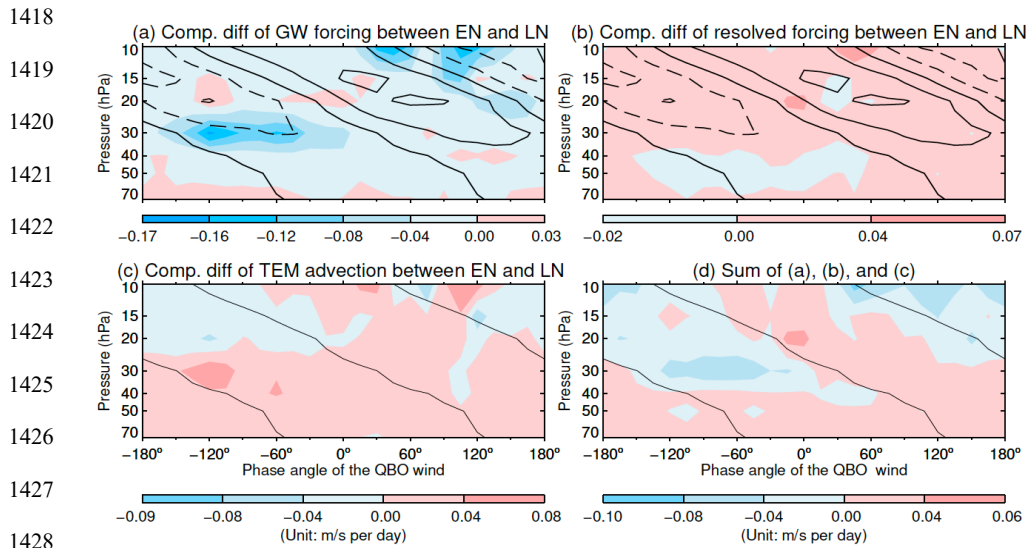
Deleted: SST anomalies



1385  
 1386 **Fig. 4.** Ensemble average of the composite QBO winds simulated by the Coupled–NINT–AP model  
 1387 during La Niña (upper panels) and El Niño (middle panels) is depicted by black contour lines where the  
 1388 contour interval is  $10 \text{ m s}^{-1}$  with dashed lines denoting negatives and solid lines denoting positives and  
 1389 zero. The location of strong shear zones of the QBO winds during ENSO extremes is delineated by the  
 1390 zero wind contour lines in lower panels. For color filled contours, left panels depict the ensemble average  
 1391 of the composite parameterized GW forcing simulated by the Coupled–NINT–AP model averaged from  
 1392  $5^\circ\text{S}$  to  $5^\circ\text{N}$  during La Niña (a) and El Niño (b) and its composite difference between El Niño and La Niña  
 1393 (c); right panels depict the ensemble average of the composite resolved wave forcing simulated by the  
 1394 Coupled–NINT–AP model during La Niña (d) and El Niño (e) and its composite difference between El  
 1395 Niño and La Niña (f).  
 1396



1411 **Fig. 5.** The black contour lines are the same as those in Fig. 4. For color filled contours, left panels depict  
 1412 the ensemble average of the composite TEM advection simulated by the Coupled-NINT-AP model  
 1413 averaged from 5°S to 5°N during La Niña (a) and El Niño (b) and the composite difference between El  
 1414 Niño and La Niña (c); right panels depict the ensemble mean totaling of the composite fields of GW  
 1415 forcing, resolved wave forcing, and TEM advection simulated by the Coupled-NINT-AP model during  
 1416 La Niña (d) and El Niño (e) and the composite difference between El Niño and La Niña (f).  
 1417

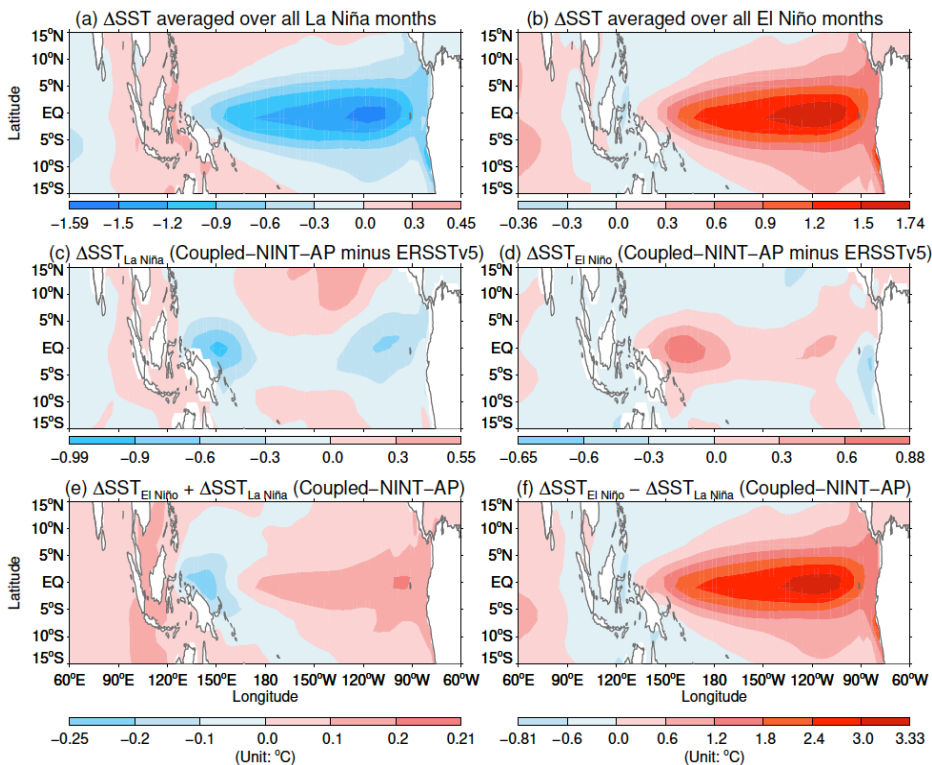


1428 **Fig. 6.** (a) and (b) are the same as the bottom panels in Fig. 4 except for the Coupled-NINT-SP model.

1429 (c) and (d) are the same as the bottom panels in Fig. 5 except for the Coupled-NINT-SP model.

1430

1431  
 1432  
 1433  
 1434  
 1435  
 1436  
 1437  
 1438  
 1439  
 1440  
 1441  
 1442  
 1443  
 1444  
 1445



1446 **Fig. 7.** Ensemble mean of the composite SSTA from the Coupled-NINT-AP runs averaged over all La  
 1447 Niña (a) and El Niño (b) months respectively over the 1871–2013 period. . Differences from observations  
 1448 are shown in (c) and (d). The sum and difference of model derived El Niño and La Niña SSTA are shown  
 1449 in (e) and (f), respectively.

Deleted: SST anomalies  
 Deleted: SST anomalies



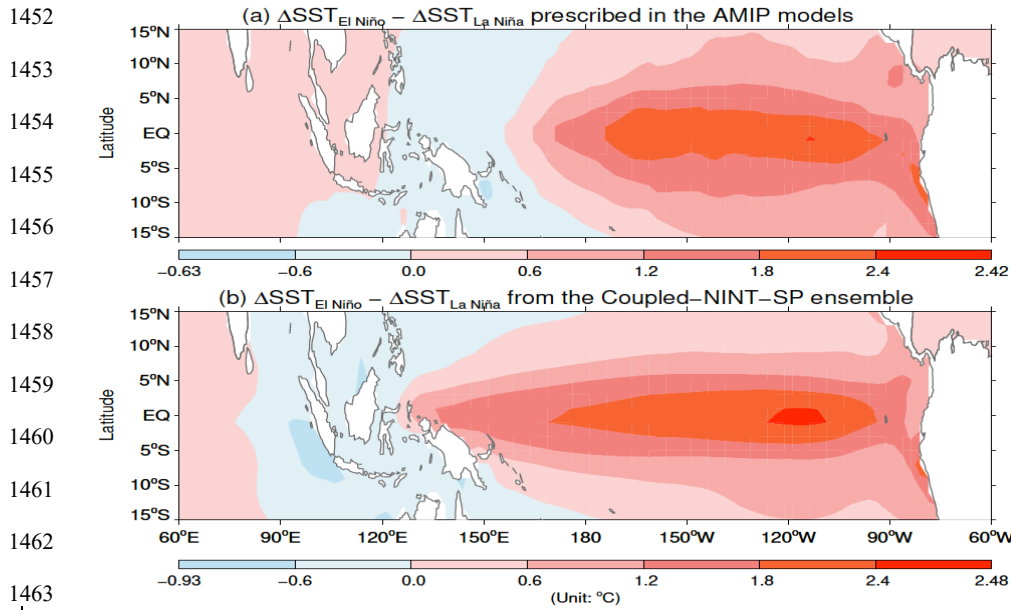
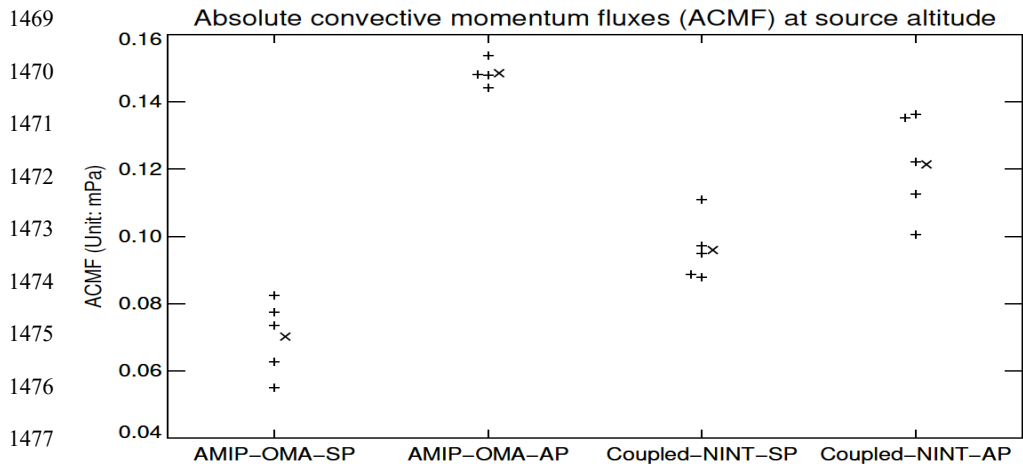


**Fig. 8.** Difference in the composite  $\Delta SSTA$  between El Niño and La Niña over the 1871–2013 period specified in the AMIP-OMA-SP and AMIP-OMA-AP models (a) and that simulated by the Coupled-NINT-SP model (b).

Deleted: SST anomalies



1478 **Fig. 9.** Difference in the composite ACMF anomalies at the source altitude averaged over the 5°S – 5°N  
 1479 latitudinal belt between El Niño and La Niña over the 1871–2013 period. Plus symbol (+) denotes the  
 1480 difference from individual runs while cross symbol (x) represents each ensemble mean difference. Some  
 1481 symbols are slightly shifted leftward or rightward to avoid overlapping with other symbols.  
 1482

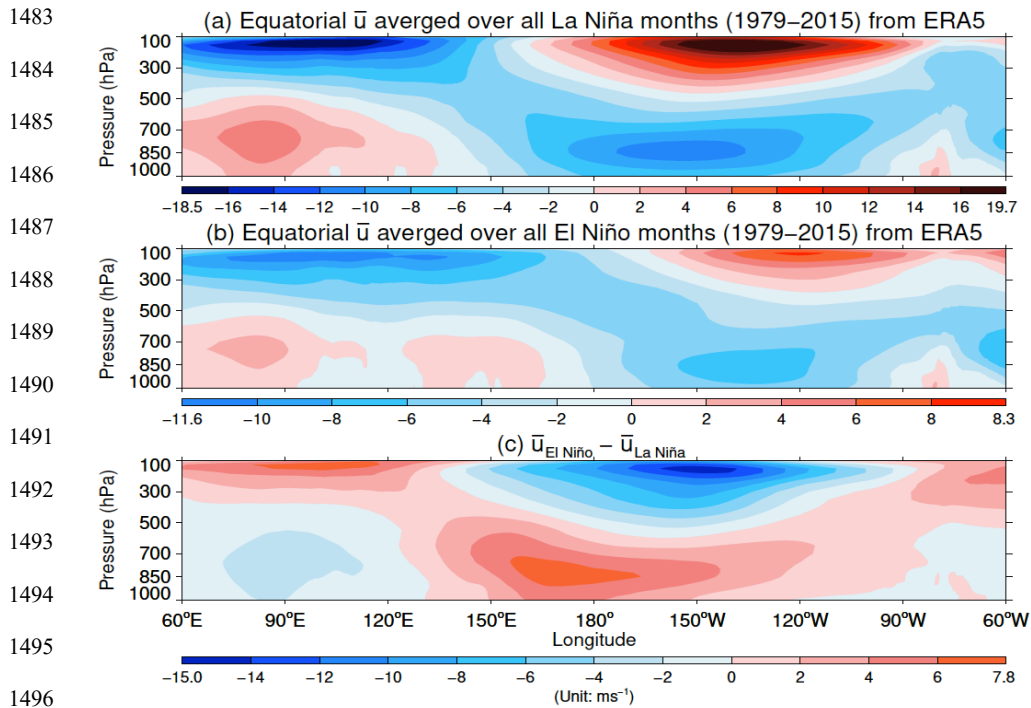
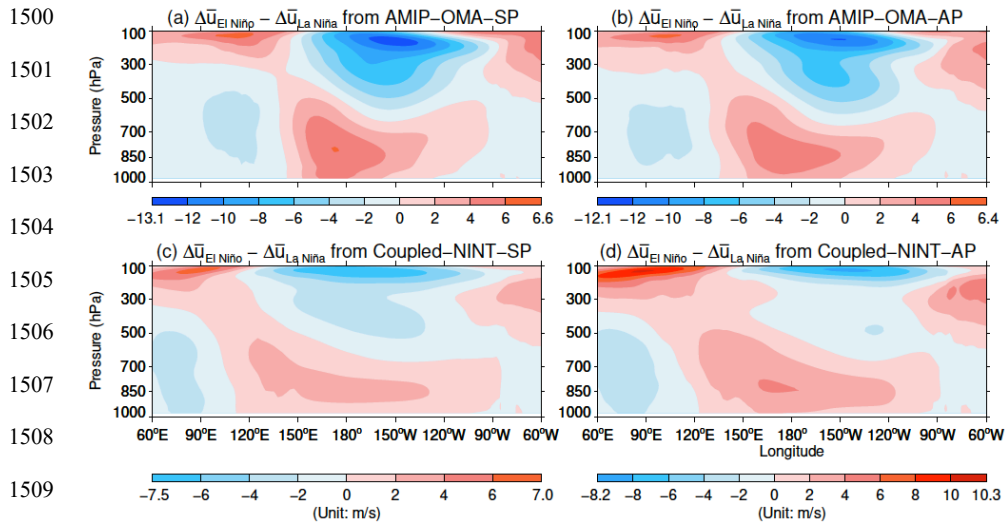


**Fig. 10.** Zonal winds from ERA5 averaged from 5°S to 5°N that are further averaged over all La Niña (a) and El Niño (b) months between 1979 and 2015 respectively, and their differences (c).



1510 **Fig. 11.** Same as Fig. 10c but for the ensemble averages of the composite difference in zonal wind  
 1511 anomalies between El Niño and La Niña simulated by AMIP-OMA-SP (a), AMIP-OMA-AP (b),  
 1512 Coupled-NINT-SP (c), and Coupled-NINT-AP (d).  
 1513

1514  
1515  
1516  
1517  
1518  
1519  
1520  
1521  
1522  
1523  
1524  
1525  
1526  
1527

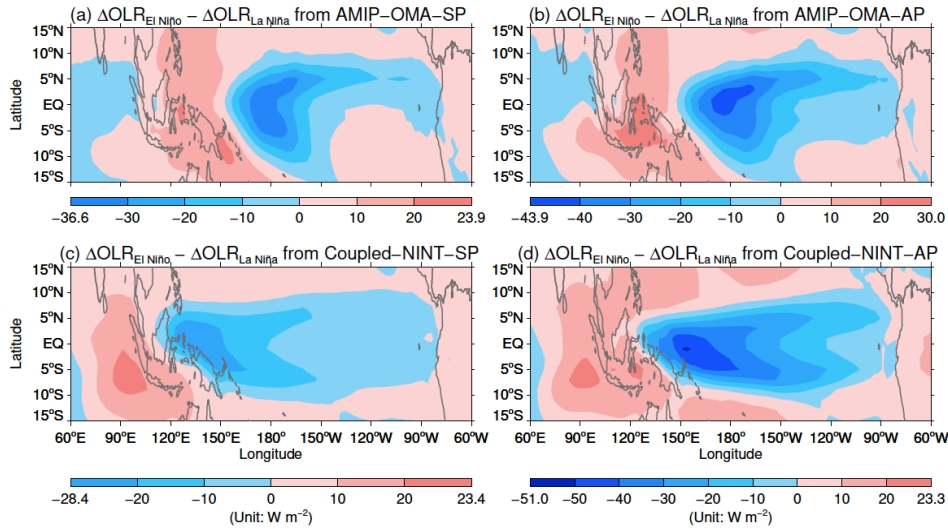
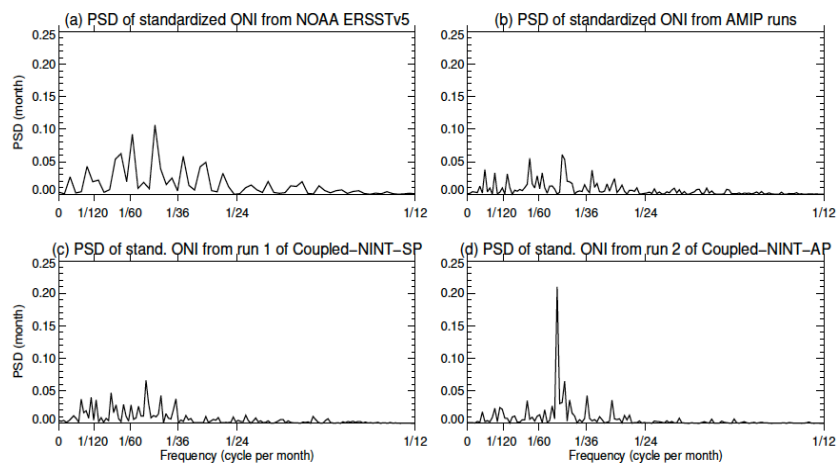


Fig. 12. Same as Fig. 11 but for the ensemble averages of the composite difference in **OLRA** between El Niño and La Niña simulated by AMIP-OMA-SP (a), AMIP-OMA-AP (b), Coupled-NINT-SP (c), and Coupled-NINT-AP (d).

Deleted: OLR anomalies

1529  
1530  
1531  
1532  
1533  
1534  
1535  
1536  
1537



1538 **Fig. 13.** Power spectral densities (PSD) of the standardized ONI between 1953 and 2015 derived from  
1539 the NOAA ERSSTv5 SST (a), of standardized ONI between 1871 and 2013 derived from the HadISST1  
1540 dataset as used in the AMIP runs (b), of standardized ONIs between 1871 and 2013 simulated by the  
1541 first realization of Coupled-NINT-SP (c) and the second realization of Coupled-NINT-AP (d),  
1542 respectively.  
1543

